This is the peer-reviewed, final accepted version for American Mineralogist, published by the Mineralogical Society of America.
The published version is subject to change. Cite as Authors (Year) Title. American Mineralogist, in press.
DOI: https://doi.org/10.2138/am-2020-7404. http://www.minsocam.org/

Revision 2 - Correction date 9 July 2020

High-pressure and high-temperature vibrational properties and anharmonicity of carbonate minerals up to 6 GPa and 500 ˚C by Raman spectroscopy

Stefan Farsang[1*], Remo N. Widmer[2] and Simon A. T. Redfern[3]

[1]Department of Earth Sciences, University of Cambridge, Downing Street, Cambridge, CB2 3EQ, UK (*sf571@cam.ac.uk)

[2]Empa, Swiss Federal Laboratories for Materials Science and Technology, Laboratory for Mechanics of Materials and Nanostructures, Feuerwerkerstrasse 39, Thun, 3602, Switzerland

[3]Asian School of the Environment, Nanyang Technological University, 50 Nanyang Avenue, Singapore, 639798, Singapore

Abstract

Carbonate minerals play a dominant role in the deep carbon cycle. Determining the high-pressure and high-temperature vibrational properties of carbonates is essential to understand their anharmonicity and their thermodynamic properties under crustal and upper mantle conditions. Building on our previous study on aragonite, calcite (both $CaCO_3$ polymorphs), dolomite [$CaMg(CO_3)_2$], magnesite ($MgCO_3$), rhodochrosite ($MnCO_3$), and siderite ($FeCO_3$) (Farsang et al. 2018), we have measured pressure- and temperature-induced frequency shifts of Raman-active vibrational modes up to 6 GPa and 500 ˚C for all naturally occurring aragonite- and calcite-group carbonate minerals, including cerussite ($PbCO_3$), strontianite ($SrCO_3$), witherite ($BaCO_3$), gaspeite ($NiCO_3$), otavite ($CdCO_3$), smithsonite ($ZnCO_3$), and spherocobaltite ($CoCO_3$). Our Raman and XRD measurements show that cerussite decomposes to a mixture of

Always consult and cite the final, published document. See http:/www.minsocam.org or GeoscienceWorld

This is the peer-reviewed, final accepted version for American Mineralogist, published by the Mineralogical Society of America.
The published version is subject to change. Cite as Authors (Year) Title. American Mineralogist, in press.
DOI: https://doi.org/10.2138/am-2020-7404. http://www.minsocam.org/

Pb_2O_3 and tetragonal PbO between 225 and 250 ˚C, smithsonite breaks down to hexagonal ZnO between 325 and 400 ˚C, and gaspeite to NiO between 375 and 400 ˚C. Spherocobaltite breaks down between 425 and 450 ˚C and otavite between 375 and 400 ˚C. Due to their thermal stability, carbonates may serve as potential reservoirs for a number of metals (e.g., Co, Ni, Zn, Cd) in a range of crustal and upper mantle environments (e.g., subduction zones). We have determined the isobaric and isothermal equivalents of the mode Grüneisen parameter and the anharmonic parameter for each Raman mode, and compare trends in vibrational properties as a function of pressure, temperature, and chemical composition with concomitant changes in structural properties. Finally, we use the anharmonic parameter to calculate the thermal contribution to the internal energy and entropy, and isochoric and isobaric heat capacity of certain carbonates.

Keywords

Anharmonicity, cerussite, diamond anvil cell, gaspeite, high pressure, high temperature, otavite, pressure sensor, Raman spectroscopy, smithsonite, spherocobaltite, strontianite, witherite

Introduction

Carbonate minerals play a dominant role in the deep carbon cycle that includes the transport of carbon bearing phases in subducting slabs to deep Earth, their devolatilization, melting, and dissolution in slab fluids, the transport of liberated CO_2, followed by volcanic outgassing (e.g., Dasgupta and Hirschmann 2010; Ague and Nicolescu 2014; Manning 2014; Kelemen and

Always consult and cite the final, published document. See http:/www.minsocam.org or GeoscienceWorld

This is the peer-reviewed, final accepted version for American Mineralogist, published by the Mineralogical Society of America.
The published version is subject to change. Cite as Authors (Year) Title. American Mineralogist, in press.
DOI: https://doi.org/10.2138/am-2020-7404. http://www.minsocam.org/

Manning 2015; Plank and Manning 2019). Carbonates transport carbon into deep Earth in three distinct lithologies (oceanic sediments, igneous crust, and lithospheric mantle). Their behavior as a function of pressure (*P*), temperature (*T*), and composition of adjacent phases determines the extent and rate of carbon recycling to the atmosphere and oceans. Modeling the deep carbon cycle therefore requires an understanding of numerous geologic processes involving carbonate minerals, which in turn depend on the thermodynamic properties of carbonates under crustal and upper mantle conditions. In all high-temperature environments (e.g., deep Earth), key thermodynamic properties of phases are dependent upon their anharmonicity. In order to obtain meaningful values for thermodynamic properties, anharmonicity and anharmonic corrections must be quantified.

The vibrational properties of a mineral control a number of its thermodynamic properties. Raman spectroscopy provides a route, therefore, to determine thermodynamic properties at the *P*-*T* conditions of measurement. As abundant CO_2-bearing minerals, the thermodynamic properties of carbonates are of particular importance. A significant number of Raman studies of the high-pressure behavior of carbonate minerals have been reported, including aragonite, calcite, vaterite, and other high-pressure $CaCO_3$ polymorphs (Fong and Nicol 1971; Nicol and Ellenson 1972; Salje and Viswanathan 1976; Liu and Mernagh 1990; Hess et al. 1991; Kraft et al. 1991; Biellmann and Gillet 1992; Gillet et al. 1993; Suito et al. 2001; Shi et al. 2012; Pippinger et al. 2015; Koch-Müller et al. 2016; Liu et al. 2017; Lobanov et al. 2017; Maruyama et al. 2017; Gavryushkin et al. 2017; Bayarjargal et al. 2018; Farsang et al. 2018; Yuan et al. 2019), azurite (Xu et al. 2015), cerussite (Lin and Liu 1997c, 1997b; Minch et al. 2010b; Zhang et al. 2013; Gao et al. 2016), dolomite (Kraft et al. 1991; Biellmann and Gillet 1992; Gillet et al. 1993; Efthimiopoulos et al. 2017, 2018; Farsang et al. 2018; Vennari and Williams 2018), ikaite

Always consult and cite the final, published document. See http:/www.minsocam.org or GeoscienceWorld

(Shahar et al. 2005), magnesite (Williams et al. 1992; Gillet 1993; Gillet et al. 1993; Spivak et al. 2014; Müller et al. 2017; Farsang et al. 2018; Liang et al. 2018a), malachite (Gao and Yuan 2020), nyerereite (Rashchenko et al. 2017), otavite (Minch et al. 2010a), rhodochrosite (Farfan et al. 2013; Liu et al. 2016; Farsang et al. 2018; Zhao et al. 2018), shortite (Borodina et al. 2018; Vennari et al. 2018), siderite (Farfan et al. 2012; Lin et al. 2012; Spivak et al. 2014; Cerantola et al. 2015; Müller et al. 2016, 2017; Farsang et al. 2018; Liang et al. 2018b), spherocobaltite (Chariton et al. 2018), strontianite (Lin and Liu 1997c, 1997b; Biedermann et al. 2017a; Efthimiopoulos et al. 2019), and witherite (Lin and Liu 1997a, 1997b; Chaney et al. 2015). High-pressure and high-temperature vibrational data have been previously combined to estimate anharmonicity and calculate thermodynamic properties of certain carbonates (Matas et al. 2000; Wang et al. 2019b).

Calcite-type carbonates are rhombohedral, space group $R\bar{3}c$, with Z = 2 formula units per primitive cell (N = 10 atoms per lattice point). The six-fold coordination of the M^{2+} metal cation by O^{2-} means they only accommodate ions with relatively small radius (Table 1). Cation ordering in dolomite-type carbonates lowers the symmetry from $R\bar{3}c$ to $R\bar{3}$. Aragonite-type carbonates are orthorhombic, space group *Pmcn*, and Z = 4, N = 20. The metal cation is coordinated by nine O atoms and they can accommodate larger divalent ions than the calcite-type carbonates (Table 1).

Here, we report pressure- and temperature-induced frequency shifts of the Raman-active vibrational modes of natural aragonite-type carbonates cerussite, strontianite, and witherite, and calcite-type carbonates gaspeite, otavite, smithsonite, and spherocobaltite up to ~6 GPa and 250-500 ˚C, respectively. To the best of our knowledge, this is the first report of high-pressure and high temperature Raman data for gaspeite, smithsonite, and spherocobaltite and high-temperature Raman data for otavite. The isobaric and isothermal equivalents of the mode Grüneisen

Always consult and cite the final, published document. See http:/www.minsocam.org or GeoscienceWorld

This is the peer-reviewed, final accepted version for American Mineralogist, published by the Mineralogical Society of America.
The published version is subject to change. Cite as Authors (Year) Title. American Mineralogist, in press.
DOI: https://doi.org/10.2138/am-2020-7404. http://www.minsocam.org/

parameters and the anharmonic parameters have been calculated along with the macroscopic Grüneisen parameter. We discuss and compare the high-pressure and high-temperature vibrational properties of these phases with those of aragonite, calcite, magnesite, rhodochrosite, and siderite presented previously (Farsang et al. 2018).

Experimental methods

Samples provided by the Natural History Museum, London were used in all experiments (Table S1). Each was characterized by electron probe microanalysis, X-ray diffraction (XRD), and Raman spectroscopy at the Department of Earth Sciences, University of Cambridge prior to investigation. The calculated chemical formulae and measured unit cell parameters are reported in Table 1.

High-pressure Raman experiments were conducted at room temperature using a membrane diamond anvil cell (Letoullec et al. 1988) equipped with type IIas diamond anvils (Almax easyLab) with culet diameters of 500 μm. A 4:1 methanol-ethanol fluid pressure-transmitting medium, hydrostatic over the full pressure range of our experiments (Klotz et al. 2009), was loaded into steel gaskets, pre-indented from an initial thickness of 240 μm to ~100 μm, then drilled with a 200 μm diameter hole, together with the sample crystal grains. Pressure was increased from ~0 to ~6 GPa in pressure increments of ~0.5 GPa using a PDS 200 pneumatic drive system (BETSA). Pressure was measured from the calibrated shift of the ruby R_1 fluorescence line (Mao et al. 1986) at least 30 minutes after each pressure change (Picard et al. 2006).

Always consult and cite the final, published document. See http:/www.minsocam.org or GeoscienceWorld

This is the peer-reviewed, final accepted version for American Mineralogist, published by the Mineralogical Society of America.
The published version is subject to change. Cite as Authors (Year) Title. American Mineralogist, in press.
DOI: https://doi.org/10.2138/am-2020-7404. http://www.minsocam.org/

High-temperature Raman experiments were performed at room pressure using a DSC600 heating stage (Linkam Scientific Instruments) with the sample held within an aluminum sample pan. The temperature was gradually increased from 25 ˚C to 250 ˚C for cerussite, 400 ˚C for otavite, 375 ˚C for smithsonite, 450 ˚C for spherocobaltite, and to 500 ˚C for the other carbonates in temperature increments of 25 ˚C. The heating rate was 5 ˚C.min^{-1} and the temperature was maintained for five minutes at each step to reach thermal equilibrium prior to data collection.

Raman data were collected from 50 to 1800 cm^{-1} using a confocal LabRAM 300 (Horiba Jobin Yvon) instrument (300 mm focal length) with spectral resolution ~1 cm^{-1}. The 532.05 nm excitation line was produced by a Ventus 532 laser source (Laser Quantum) focused on the sample using a M Plan Apo SL 50× (Mitutoyo) long working distance objective for the high-pressure experiments and an LMPLFLN 50× (Olympus) long working distance objective for the high-temperature experiments. All spectra were treated by PeakFit™ software. For each, the baseline was subtracted, and peaks fitted using Voigt profiles. Spectra were calibrated against the measured excitation of a Ne light reference (Saloman and Sansonetti 2004).

In situ high-temperature (ambient pressure) XRD experiments were conducted to investigate carbonate decomposition products using two Bruker D8 ADVANCE instruments equipped with either an MRI or an Anton Paar HPC900 heating stage (Table S2).

Results and Discussion

Raman-active modes of aragonite-group carbonate minerals

Always consult and cite the final, published document. See http:/www.minsocam.org or GeoscienceWorld

Aragonite, cerussite, strontianite, and witherite possess 3N – 3 = 57 optical modes. Based on nuclear site group analysis, the irreducible representations of these modes at the Brillouin Zone center, Γ, are

$$\Gamma = 9A_g + 6A_u + 6B_{1g} + 8B_{1u} + 9B_{2g} + 5B_{2u} + 6B_{3g} + 8B_{3u}$$

of which the A_g, B_{1g}, B_{2g}, and B_{3g} modes (30 in total) are Raman-active. Due to variations and anisotropy in polarizability, the intensity of certain modes may vary significantly depending on the crystallographic orientation. In certain orientations some bands may be absent. Therefore, ten spectra of crystals in different orientations were collected for each carbonate. However, the assessment of orientation and polarization effects is beyond the scope of this study. Of the 30 expected Raman-active modes, 20 were observed for aragonite at 25 ˚C (Farsang et al. 2018), and 21, 23, and 17 for strontianite, cerussite, and witherite, respectively (Figure 1).

The low-frequency (< 300 cm^{-1}) external modes associated with lattice vibrations include rotations and translations of the M^{2+} ions (M being Ca, Sr, Pb, and Ba, respectively) and CO_3^{2-} groups (Couture 1947). Aragonite shows 13 such external modes, while there are 12 in cerussite and strontianite, and 11 in witherite (Figure 1). At elevated *P*, two additional low-frequency bands were seen for cerussite with extrapolated ambient *P* frequencies 63 and 67 cm^{-1}, respectively.

The high-frequency (> 650 cm^{-1}) internal modes of the CO_3^{2-} group include the ν_4 in-plane bendings around ~700 cm^{-1}, the ν_2 out-of-plane bending around ~840 cm^{-1}, the ν_1 C–O stretching around ~1070 cm^{-1}, and the ν_3 C–O stretchings above 1300 cm^{-1} (Couture 1947; Carteret et al. 2013). The frequencies of the ν_1 modes of the three alkali earth orthorhombic carbonates correlate well with ionic radii and M–O bond lengths (Figure 2). The ν_2 satellite band at 824 cm^{-1} seen for cerussite and the ν_1 satellite bands at 1059, 1050, 1031, and 1038 cm^{-1} in

Always consult and cite the final, published document. See http:/www.minsocam.org or GeoscienceWorld

aragonite, strontianite, cerussite, and witherite, respectively are assigned to isotopic substitutions of ^{13}C and ^{18}O (Cloots 1991; Martens et al. 2004). The frequencies of each of the internal modes decrease in the order of aragonite > strontianite > witherite (although the frequency of the ν_2 mode is very similar in aragonite and strontianite) as predicted from the relative cation size (Ca^{2+} < Sr^{2+} < Ba^{2+}). Despite Pb^{2+} being smaller than Ba^{2+} (1.35 vs. 1.47 Å in nine-fold coordination, Shannon 1976), cerussite has the lowest frequency internal modes of the four aragonite-group carbonates. Our data confirm the general trend of frequency (aragonite > strontianite > witherite > cerussite) noted in earlier works (Wang et al. 2019a and references therein).

Raman-active modes of calcite-group carbonate minerals

Calcite, gaspeite, magnesite, otavite, rhodochrosite, siderite, smithsonite, and spherocobaltite have 3N – 3 = 27 optical modes. The irreducible representations of these modes at the Brillouin Zone center, Γ, are

$$\Gamma = A_{1g} + 2A_{1u} + 3A_{2g} + 3A_{2u} + 4E_g + 5E_u$$

of which the A_{1g} and E_g modes (five in total) are Raman-active. All of these were observed in the Raman spectra of calcite-group carbonates at 25 ˚C, except that one of the E_g modes was absent for siderite (Figure 3 and Table 2).

The translational (T) E_g lattice mode corresponds to translation of the CO_3 groups (Bischoff et al. 1985; Liu and Mernagh 1990). T modes frequencies correlate well with ionic radii and M–O bond lengths (Figure 4), with similar values to those previously reported (Dufresne et al. 2018). The librational (L) E_g lattice mode arises from librations of the CO_3 groups (Bischoff et al. 1985; Liu and Mernagh 1990). The L mode frequencies correlate

Always consult and cite the final, published document. See http:/www.minsocam.org or GeoscienceWorld

moderately well with ionic radii (Figure 4), in agreement with the earlier observations of Dufresne et al. (2018).

The high-frequency (700-1500 cm^{-1}) bands are internal modes of the CO_3^{2-} group (Couture 1947). They include the ν_4 E_g asymmetric in-plane bending mode, the highest intensity ν_1 A_{1g} symmetric C–O stretching mode, and the ν_3 E_g asymmetric C–O stretching mode. We do not find a strong correlation between ν_1 frequencies and ionic radii or M–O bond distances (Figure 4) in contrast to Dufresne et al. (2018).

The highest-frequency (> 1700 cm^{-1}) band represents either the $2\nu_2$ overtone mode of the IR active ν_2 A_{2u} mode (Krishnan 1945; Couture 1947; Krishnamurti 1957; De La Pierre et al. 2014) or the ν_1 A_{1g} + ν_4 E_g combination mode (Rutt and Nicola 1974; Herman et al. 1987). We prefer the former interpretation based on the simple observation that this band, just like the IR-active ν_2 band (Santillán and Williams 2004), shows close to 0 or negative shift with *P*, in contrast to the other observed Raman-active modes.

An additional broad, low-intensity feature occurs at 507 cm^{-1} for siderite. This is caused by an Fe^{2+} electronic excitation (Popkov et al. 1972). We did not observe the broad feature of unknown origin reported by Chariton et al. (2018) at 1970 cm^{-1} in their study of spherocobaltite.

High-pressure spectra of aragonite-group carbonates

In aragonite, strontianite, cerussite, and witherite 15, 16 (including a satellite), 21 (including a satellite), and 14 modes, respectively, could be traced over at least part of the measured pressure range. Their frequency evolutions as a function of pressure (Figure 5 and Figure S1 and

Always consult and cite the final, published document. See http:/www.minsocam.org or GeoscienceWorld

Supplementary Material 1) are, to first degree, linear and $\delta\nu_i/\delta P$ for all modes are effectively constant over the observed pressure range (Table S3).

For all carbonates studied, the pressure-induced shifts of internal modes are generally smaller than those of the external modes due to the greater incompressibility of the CO_3 units (Ross and Reeder 1992; Gillet et al. 1993) (Figure 5). The frequencies of all external modes increase with pressure, except the lowest-frequency bands in aragonite and strontianite. In all carbonates, three ν_4 in-plane bending modes could be traced, with positive $\delta\nu_i/\delta P$. The site group splitting of ν_4 bands increases with pressure, indicating increasing distortion of the CO_3 units (White 1974 and references therein). The inverse relationship between the magnitude of ν_4 band splitting and cation size described by White (1974) is seen in all samples except cerussite, which displays much larger ν_4 band splitting than other carbonates. The ν_2 out-of-plane bending mode and its satellite could only be traced in cerussite and they have similar negative $\delta\nu_i/\delta P$. The ν_1 C–O stretching mode showed positive $\delta\nu_i/\delta P$ in all samples. The ν_1 satellite band was only traced (up to ~5 GPa) in strontianite, with $\delta\nu_i/\delta P$ similar to the ν_1 band. One ν_3 C–O stretching mode could be traced in aragonite, two in strontianite and witherite, and three in cerussite. All ν_3 bands have positive $\delta\nu_i/\delta P$. Slightly increased splitting of ν_3 bands with pressure was only observed in witherite, indicative of increasing distortion of the CO_3^{2-} units in the CO_3^{2-} plane (Greenaway et al. 1986; Kraft et al. 1991). The splitting of ν_3 bands showed little variation in strontianite and cerussite.

Beyond the simple dependence on instrumental resolution, the linewidth of a Raman peak is inversely dependent upon phonon lifetime. Hence it generally increases with temperature and linewidth may also reflect phonon – point defect scattering associated with either trace element incorporation or other defect accumulation. The ν_1 modes in aragonite-group carbonates have

Always consult and cite the final, published document. See http:/www.minsocam.org or GeoscienceWorld

narrow linewidths, below 4 cm^{-1} over the studied pressure range (Figure S1). Linewidths of other modes were not determined due to overlaps and/or low-intensity peaks.

High-pressure spectra of calcite-group carbonates

The frequency-evolution of all Raman-active modes in the calcite-group carbonates could be traced over the entire pressure range of our experiments with the exception of those for calcite (Farsang et al. 2018). The ambient pressure and temperature $R\bar{3}c$ phase of calcite (calcite I) undergoes a ferroelastic symmetry-breaking structural phase transition to calcite II on increasing pressure through ~1.4 GPa, with a subsequent transition to calcite III at ~1.7 GPa (Bridgman 1938). The Raman-active modes of calcite I could only be traced up to the pressure corresponding to the first transition, therefore (Farsang et al. 2018). The frequency-evolution of all calcite-group carbonate modes as a function of pressure is reported in Figure 6 and Figure S2 and Supplementary Material 1 and the relative changes in frequency $\delta\nu_i/\delta P$ are given along with earlier reported values in Tables 3 and S4. We find $\delta\nu_i/\delta P$ for all modes is effectively constant over the observed pressure range, with linear changes in the pressure dependence of mode frequencies. All measured Raman peaks increase in frequency with pressure, with the exception of the Fe^{2+} electronic excitation feature seen in siderite and the overtone mode in certain calcite-group carbonates. Calcite has the lowest $\delta\nu_i/\delta P$ of T mode and the highest $\delta\nu_i/\delta P$ of L and ν_1 modes. The extreme values are likely associated with the structural transition of calcite occurring at and above ~1.4 GPa. The close to 0 or negative slope of the highest frequency mode supports the interpretation that this is the $2\nu_2$ overtone of ν_2 out-of-plane bending mode of the CO_3 group rather than the $A_{1g} + E_g$ combination mode. The negative $\delta\nu_i/\delta P$ of the $2\nu_2$ overtone mode has

Always consult and cite the final, published document. See http:/www.minsocam.org or GeoscienceWorld

been related to the distortion of MO_6 octahedra (Liang et al. 2018b). Carbonates with large cations (e.g., Fe^{2+}, Mn^{2+}, Cd^{2+}, Ca^{2+}) show a larger negative $\delta\nu_i/\delta P$ of $2\nu_2$ indicating a more significant MO_6 octahedral distortion.

Due to the large uncertainty arising from peak fitting, it is difficult to discern changes in linewidth of T and L modes (Figure S2). The linewidth of the ν_1 mode is much broader in calcite-group carbonates than in the aragonite-group carbonates (Figure S2). It decreases with *P* in carbonates with small cations (e.g., magnesite, gaspeite), but remains quasi-constant or increases in carbonates with larger cations. Once again, carbonates with large cations likely experience greater distortions of MO_6 octahedra and CO_3 units that connect these polyhedra, resulting in broader ν_1 peaks.

High-temperature spectra of aragonite-group carbonates

In aragonite, strontianite, cerussite and witherite, 20 (including a satellite), 13 (including a satellite), 16 (including a satellite), and 15 modes, respectively, could be traced over (at least part of) the observed temperature range. The temperature-dependence of the frequency of modes in these aragonite-group carbonates (Figures 7, S3 and Supplementary Material 2) is linear and the values of $\delta\nu_i/\delta T$ (Table S3) are, to first approximation, constant over the observed temperature range. In both aragonite and calcite-group carbonates, the temperature-induced shifts of internal modes are generally smaller than those of the external modes, due to the rigidity of C−O bonds in the CO_3 units (Markgraf and Reeder 1985; Reeder and Markgraf 1986; Gillet et al. 1993). All external modes decrease in frequency with temperature. In aragonite, strontianite, and witherite, some bands appear to cross or merge at elevated temperatures, become indistinguishable from

Always consult and cite the final, published document. See http:/www.minsocam.org or GeoscienceWorld

one another and were therefore further treated as one band. Three ν_4 bands could be traced in aragonite, cerussite, and witherite, but only two were seen in strontianite; all show positive $\delta\nu_i/\delta T$ for all samples. In aragonite and witherite, the highest frequency ν_4 band decreases in intensity on heating, while the two lower frequency ν_4 bands merge into one at 250 and 300 ˚C, respectively. In contrast to the work of White (1974), we observed ν_4 site group splitting in all aragonite-group carbonates. The converging nature of ν_4 bands, i.e. decreasing site group splitting with increasing temperature, is interpreted as a symmetry change in the local crystal field surrounding the CO_3 group, or as a decrease in distortion of the CO_3 group itself (Gillet et al. 1993). The ν_2 band could only be traced in aragonite, strontianite, and cerussite and has a negative $\delta\nu_i/\delta T$ in all carbonates. The ν_1 band has negative $\delta\nu_i/\delta T$ in all carbonates. Its satellite band could only be measured for aragonite, strontianite, and cerussite up to 250, 300, and 175 ˚C, respectively. The $\delta\nu_i/\delta T$ of satellite bands are very similar to those of ν_1 bands. Two ν_3 bands could be traced over at least part of the observed temperature range and show negative $\delta\nu_i/\delta T$ in all carbonates. Among all samples, only strontianite showed slightly decreasing splitting of ν_3 bands on heating, suggesting decreasing distortion of the CO_3^{2-} units within the CO_3^{2-} plane (Greenaway et al. 1986; Kraft et al. 1991). The splitting of ν_3 bands is near-constant in other aragonite-group carbonates. In general, $\delta\nu_i/\delta T$ values of ν_4 modes are greater (positive or less negative) than those of ν_2, which are greater (less negative) than those of ν_1, which are in turn greater (less negative) than those of ν_3, in agreement with the observations of Wang et al. (2019a).

At ambient pressure and above 425 ˚C, aragonite transforms to calcite. The modes of aragonite could only be traced below this temperature, therefore (Figure S4). The thermal decomposition of cerussite to Pb-oxide(s) and presumably CO_2 was observed between 225 and

Always consult and cite the final, published document. See http:/www.minsocam.org or GeoscienceWorld

250 ˚C (Figure S5). At 250 ˚C, Raman peaks characteristic to cerussite are no longer visible. Instead, new peaks appear at 84, 136, 268, and 367 cm^{-1}, indicative of PbO (Cortez-Valadez et al. 2013). In contrast, *in situ* high-temperature XRD revealed the presence of two decomposition products, Pb_2O_3 and minor tetragonal PbO (litharge). Both these results are in sharp contrast to the observed melting of cerussite observed at 570 K (297 ˚C) by Wang et al. (2019a). The widths of ν_1 modes increase significantly with temperature (Figure S3). Linewidths of other modes were not determined due to overlaps and/or low-intensity peaks.

High-temperature spectra of calcite-group carbonates

The frequency evolution of all Raman modes from calcite-group carbonates could be traced over the observed temperature range with the exception of the ν_3 E_g mode in spherocobaltite, the Fe^{2+} electronic excitation feature in siderite, and the ν_4 E_g mode in otavite due to the decreasing intensity of these peaks. The frequency of all measured modes decrease or remain constant with increasing temperature (Figure 8 and Figure S6 and Supplementary Material 2) and $\delta\nu_i/\delta T$ for all modes is approximately constant over the observed temperature range (Tables 4 and S4). In smithsonite, gaspeite and siderite, $\delta\nu_i/\delta T$ for ν_1 decreases rapidly above 200 ˚C. In rhodochrosite and otavite, $\delta\nu_i/\delta T$ for ν_1 shows significant fluctuation. Gillet et al. (1993) noted that in calcite (and presumably in other calcite-group carbonates too), the changes in frequency of the ν_1 mode are not primarily due to changes in bond length or polyhedral volume, but rather due to increasing distortion as the O–O distance in the basal plane of the CaO_6 octahedra shortens. Similar to aragonite-group carbonates, $\delta\nu_i/\delta T$ for ν_4 is greater (positive or less negative) than that

Always consult and cite the final, published document. See http:/www.minsocam.org or GeoscienceWorld

for ν_1 (except in magnesite and siderite). Furthermore, $\delta\nu_i/\delta T$ for ν_1 is greater (less negative), than that for ν_3.

In general, the linewidths of T, L, and ν_1 modes in the calcite-group carbonates increase with temperature (Figure S6). In calcite, a nonlinear increase in width of the T mode peak occurs above 400 ˚C, as noted by Gillet et al. (1993). They related the quasi-linear increase up to 400 ˚C to the simple volume thermal expansion associated with a cubic anharmonicity term (Brehat and Wyncke 1985) and the anomalous increase above 400 ˚C to additional anharmonic terms associated with the relaxational mode, before the onset of rotational order-disorder transition at higher temperatures (Megaw 1970; Redfern et al. 1989). In gaspeite, the large linewidth of the ν_1 mode may be a consequence of compositional heterogeneity and the existence of Mg-rich domains in the sample.

The thermal decomposition of gaspeite to NiO (and presumably CO_2) commences above 375 and is complete below 400 ˚C (Figure S7). The broad peaks at 525 and 1075 cm^{-1} correspond to one-phonon (1P) TO and LO modes and two-phonon (2P) 2LO modes of NiO, respectively (Dietz et al. 1971). At room temperature, NiO exhibits its highest intensity two-magnon (2M) scattering band at ~1500 cm^{-1} but (being well above the Néel temperature of NiO) this band becomes unidentifiable in our spectra (Dietz et al. 1971). The gradual thermal decomposition of smithsonite starts above 325 and is complete below 400 ˚C (Figure S8). This temperature range is slightly higher than that reported by Hales and Frost (2008). Our *in situ* high-temperature XRD experiments indicate that the decomposition product is hexagonal ZnO and presumably CO_2. In the spectrum collected at 400 ˚C bands corresponding to smithsonite are absent. The high-intensity peaks at 102, 325, 433, and 573 cm^{-1} indicate the presence of hexagonal ZnO (Decremps et al. 2002). The thermal decomposition of spherocobaltite was

Always consult and cite the final, published document. See http:/www.minsocam.org or GeoscienceWorld

observed between 425 and 450 ˚C and the decomposition of otavite between 375 and 400 ˚C, marked by the disappearance of all its Raman bands. The latter temperature range is slightly higher than the previously suggested range of 330-375 ˚C (Ballirano 2016), probably due to the trace element content of our otavite. Gaspeite, otavite, and spherocobaltite showed increased sensitivity under the laser beam at higher temperatures and it was necessary to decrease the laser power at temperatures starting at 375, 350, and 200 ˚C, respectively. The sensitivity of spherocobaltite to laser beam damage has also been reported elsewhere (Rutt and Nicola 1974). For comparison, the decomposition of rhodochrosite takes place between 400 and 425 ˚C, while the decomposition of siderite occurs between 375 and 400 ˚C (Farsang et al. 2018).

Mode Grüneisen and intrinsic anharmonic parameters

While pressure-induced frequency shifts of a given vibrational mode arise from the implicit pure volume contribution due to compressibility, temperature-induced frequency shifts of a given vibrational mode arise from two contributions: (1) the implicit, pure volume contribution due to thermal expansion and (2) the explicit, volume independent, phonon-excitation contribution due to phonon-phonon interactions, known as intrinsic anharmonicity (Gervais et al. 1973; Peercy and Morosin 1973; Gillet et al. 1989, 1998). The isobaric and isothermal equivalents of the mode Grüneisen parameter and the intrinsic anharmonic parameter provide the means to quantify these contributions.

The mode Grüneisen parameter, γ_i, links the change in frequency of vibrational mode i, ν_i (measured at 25 ˚C in this work), to the change in volume V (Born and Huang 1954):

$$\gamma_i = -\frac{d \ln \nu_i}{d \ln V} = -\frac{V d\nu_i}{\nu_i dV}$$

Always consult and cite the final, published document. See http:/www.minsocam.org or GeoscienceWorld

The isobaric equivalent of mode Grüneisen parameter, γ_{iP} (Gillet et al. 1989) describes the temperature dependence of the vibrational mode and can be expressed as:

$$\gamma_{iP} = -\frac{d \ln \nu_i}{d \ln V\,(T)} = -\frac{d\nu_i}{\alpha \nu_i dT}$$

where α is the thermal expansion coefficient. The isothermal equivalent of mode Grüneisen parameter, γ_{iT} (Gillet et al. 1989; Wagner 2000) describes the pressure dependence of the vibrational mode and can be expressed as:

$$\gamma_{iT} = -\frac{d \ln \nu_i}{d \ln V\,(P)} = \frac{K_T d\nu_i}{\nu_i dP}$$

where K_T is the isothermal bulk modulus. From the difference between γ_{iT} and γ_{iP}, the intrinsic anharmonic parameter, a_i, quantifying intrinsic anharmonicity, can be calculated for each mode (Gillet et al. 1989):

$$a_i = \alpha(\gamma_{iT} - \gamma_{iP})$$

The isobaric and isothermal equivalents of the Grüneisen parameter and the anharmonic parameter have been calculated for each measured mode using thermodynamic properties reported in Table 5 and are presented in Table S3 and Figure S9 for aragonite-group carbonate minerals and Table S4 and Figure S10 for calcite-group carbonate minerals. Values of the isobaric and isothermal equivalents of the Grüneisen parameter and the anharmonic parameter span a much larger range for external modes than internal modes in both aragonite and calcite-group carbonate minerals. As a consequence, external modes are expected to contribute significantly more to the intrinsic anharmonicity.

In aragonite-group carbonates, values of γ_{iP} of external modes range from 0.14 to 4.10, γ_{iT} from -0.69 to 4.75, and a_i from -17.33 to 36.92. The values of γ_{iP} of internal modes range from -0.13 to 0.39, γ_{iT} from 0.07 to 0.26, and a_i from -1.44 to 1.83. In aragonite-group carbonates, the

Always consult and cite the final, published document. See http:/www.minsocam.org or GeoscienceWorld

values of γ_{iP} generally increase with increasing frequency of internal vibrational modes, i.e. they are smaller for the ν_4 and ν_2 bending modes than for the ν_1 and ν_3 stretching modes of the CO_3 groups, a result consistent with earlier observations and implying a lower sensitivity of O–C–O angles to temperature than the C–O bond length (Wang et al. 2019a). At the same time, a_i values generally decrease with increasing frequency of internal modes. In contrast to earlier results, our γ_{iP} values for the external vibrational modes of cerussite were not lower than those of other aragonite-group carbonates (Wang et al. 2019a). However, γ_{iT} values were higher, in agreement with the same study.

In the calcite-group carbonates, the values of γ_{iP} of the external modes range from -0.15 to 12.89, γ_{iT} from 1.12 to 2.54, and a_i from -15.29 to 8.03. The values of γ_{iP} for the internal modes range from -0.09 to 1.28, γ_{iT} from 0.22 to 0.55, and a_i from -1.29 to 0.94. In calcite-group carbonates, γ_{iP} values generally increase with increasing frequency of the internal modes, i.e. they are smaller for the ν_4 bending mode than for ν_1 and ν_3 stretching modes of CO_3 groups, a result consistent with earlier observations of aragonite-group minerals and implying lower sensitivity of O–C–O angles to temperature than C–O bond length (Wang et al. 2019a). At the same time, a_i values generally decrease with increasing frequency of the internal modes.

Published ν_i, $\delta\nu_i/\delta P$, $\delta\nu_i/\delta T$, γ_{iT}, γ_{iP}, and a_i values corresponding to the same Raman-active modes of any particular carbonate mineral show considerable variation. The possible reasons for the variation in measured ν_i, $\delta\nu_i/\delta P$, and $\delta\nu_i/\delta T$ values include trace element content and the use of different pressure transmitting media. Due to differences in the ion size and mass, substitution will change the average inter-atomic distances and bond strengths and, consequently, the frequency of vibrational modes (Krishnamurti 1956; Rutt and Nicola 1974). As large (e.g., CaO_6) octahedra are more compressible than small (e.g., MgO_6) octahedra (Ross and Reeder

Always consult and cite the final, published document. See http:/www.minsocam.org or GeoscienceWorld

This is the peer-reviewed, final accepted version for American Mineralogist, published by the Mineralogical Society of America.
The published version is subject to change. Cite as Authors (Year) Title. American Mineralogist, in press.
DOI: https://doi.org/10.2138/am-2020-7404. http://www.minsocam.org/

1992), trace element content will also affect $\delta v_i/\delta P$ values. The complex effects of temperature on the structure of carbonates with different ions (e.g. Markgraf and Reeder 1985; Reeder and Markgraf 1986), will result in a range of $\delta v_i/\delta T$ values too. The use of different pressure transmitting media (e.g., Ne, methanol-ethanol, KBr), some of which may not sustain hydrostatic pressure in the pressure range of measurements, may lead to different $\delta v_i/\delta P$ values as shown by the example of magnesite (Liang et al. 2018a). Differences in γ_{iT}, γ_{iP}, and a_i can be further amplified by the use of different literature values of thermodynamic parameters for the calculation.

Macroscopic Grüneisen parameter

The macroscopic Grüneisen parameter, γ_{th}, accounts for all contributions of the mode Grüneisen parameter and can be calculated as:

$$\gamma_{th} = \frac{\alpha K_S}{\rho C_P} = \frac{\alpha K_T}{\rho C_V}$$

where α is the thermal expansion coefficient, K_S and K_T are the adiabatic and isothermal bulk moduli, respectively, ρ is the molar density, and C_P and C_V are the heat capacities at constant pressure and volume, respectively. The macroscopic Grüneisen parameters calculated for individual carbonate minerals are reported in Table 5.

Comparison with structural data

Previous XRD studies have shown that all four aragonite-group carbonate minerals display anisotropic linear compression (Martinez et al. 1996; Wang et al. 2015; Gao et al. 2016)

Always consult and cite the final, published document. See http:/www.minsocam.org or GeoscienceWorld

and anisotropic thermal expansion (Ye et al. 2012), the compression and thermal expansion along the *z* axis being much larger than that along *x* and *y* axes. This behavior can be explained by the much more sensitive M–O bond distance compared to the C–O bond distance, which is almost constant with pressure (Li et al. 2015) and temperature (Antao and Hassan 2010; Ye et al. 2012), and the orientation of nearly planar CO_3^{2+} groups, in which the C–O bonds lie, perpendicular to *z* axis. In isostructural solids, compressional behavior can be explained either by the size, charge, or electronic configuration of the constituent atoms, in our case limited to the M^{2+} ion (Zhang and Reeder 1999). The size of M^{2+} ions varies considerably (Table 1), the charge is the same, and there are two types of electronic configuration present: p^6 closed-shell configuration present in Ca^{2+}, Sr^{2+}, and Ba^{2+} as opposed to the $6s^2$ lone pair of Pb^{2+} (Table 1). Plotting bulk modulus values against unit cell (or molar) volume reveals that compressibility is directly proportional to the unit cell volume in aragonite-group carbonate minerals having an alkaline earth element M^{2+} ion, while cerussite has lower compressibility than its unit cell volume implies (Wang et al. 2015). In addition, the thermal expansion along the *z* axis is much larger for cerussite than for the other carbonate minerals and there is also a larger variation (increase) in c/c_0 values with increasing temperature (Ye et al. 2012). The significantly higher thermal expansion coefficient of cerussite compared to other aragonite-group carbonates (Ye et al. 2012) indicates that size alone cannot account for the thermal behavior of aragonite-group carbonates. Instead, a possible reason suggested for the anomalous behavior of cerussite is its electronic configuration, but no further explanation was given (Minch et al. 2010b). A detailed account based on the extremely high electronegativity of Pb^{2+} (Table 1) was given by Gao et al. (2016). According to this, the high electronegativity implies additional metalloid behavior, adding some covalent character to the Pb–O bond, which, due to its directional nature, may

Always consult and cite the final, published document. See http:/www.minsocam.org or GeoscienceWorld

restrict the movement of CO_3^{2-} groups in the structure. These behave as rigid bodies with only slight changes of O–C–O bond angles with pressure (Li et al. 2015), a result consistent with the distortion of CO_3^{2-} groups reflected in splitting of internal modes as seen in this study and elsewhere (Kraft et al. 1991).

The frequency of the most intense ν_1 band decreases with increasing unit cell volume in alkaline earth aragonite-group carbonates, while the frequency of the ν_1 band of cerussite is lower than expected (Figure 9a). The pressure-induced shift of the ν_1 band decreases with increasing unit cell volume in the three alkaline earth aragonite-group carbonates (Figure 9b). Once again, the pressure-induced shift of ν_1 band of cerussite is slightly lower than implied by the general trend. The pressure-induced shift of the ν_1 band decreases with compressibility too (Figure 9c). Cerussite is once more an outlier indicating that the electron configuration and electronegativity of Pb^{2+} affects both structural and vibrational properties. The three alkaline earth aragonite-group carbonate minerals show no systematic trend between thermal expansion coefficient and unit cell volume. Similarly, no trends were observed between the $\delta\nu_i/\delta T$ of ν_1 band and unit cell volume and between the $\delta\nu_i/\delta T$ of ν_1 band and thermal expansion coefficient.

Calcite-group carbonate minerals also display anisotropic compression (Redfern et al. 1993; Redfern and Angel 1999; Zhang and Reeder 1999; Redfern 2000; Liang et al. 2018b) and anisotropic thermal expansion (Wang et al. 2018), the compression and thermal expansion along *z* axis (in the hexagonal setting) being much larger than that along *x* axis. While the compressibility along *z* axis is nearly linear with M–O bond length in calcite-group carbonate minerals, compressibility along the *x* axis shows large differences depending on the cation type (Zhang and Reeder 1999). Systematic compressibility behavior, expressed as bulk modulus versus unit cell volume, is limited to subsets of carbonate minerals sharing metal ions of similar

Always consult and cite the final, published document. See http:/www.minsocam.org or GeoscienceWorld

valence state: alkaline earth elements with p^6 closed-shell configuration, 3d transition metals, and a 4d transition metal (Zhang and Reeder 1999, Table 1). Systematic trends in thermal expansion across calcite-group carbonate minerals are unclear. There is no clear relationship between unit cell volume and thermal expansion along the *z* axis (Wang et al. 2018). Markgraf and Reeder (1985) reported a positive thermal expansion along *x* for magnesite and a negative one for calcite, in agreement with Wang et al. (2018), who reported a positive thermal expansion along the *x* axis for magnesite, rhodochrosite, and smithsonite, a positive thermal expansion along the *x* axis for otavite over the range 123 – 223 K (-150 – -50 ˚C), followed by a negative one between 223 and 593 K (-50 – 320 ˚C), and a negative thermal expansion along the *x* axis for calcite between 123 and 618 K (-150 – 345 ˚C). The negative thermal expansion along the *x* axis for calcite was explained in terms of the shortening of the C–O bond and the basal edge O_1–O_2 bond distances due to the large libration of the CO_3^{2-} unit (Markgraf and Reeder 1985). The libration of the CO_3^{2-} unit is expected to increase with ion size, explaining why only carbonates with large ions (e.g., Ca^{2+} and Cd^{2+}) show negative thermal expansion along the *x* axis (Wang et al. 2018). An inverse correlation between thermal expansion along the *x* axis and the M^{2+} cation radius was found by Wang et al. (2018).

In contrast to aragonite-group carbonate minerals, systematic trends in the subgroups of calcite-group carbonate minerals having cations of similar electronic configuration (i.e., alkali earth elements, 3d and 4d transition metals) are difficult to observe for a number of reasons. There are only two alkaline earth calcite-group minerals (calcite and magnesite) and only one 4d transition metal calcite-group carbonate (otavite) and although there are five 3d transition metal calcite-group carbonates, they have different numbers of electrons (and paired electrons) in their outer shell, which may complicate general trends in their behavior.

Always consult and cite the final, published document. See http:/www.minsocam.org or GeoscienceWorld

This is the peer-reviewed, final accepted version for American Mineralogist, published by the Mineralogical Society of America.
The published version is subject to change. Cite as Authors (Year) Title. American Mineralogist, in press.
DOI: https://doi.org/10.2138/am-2020-7404. http://www.minsocam.org/

Regardless of the electronic configuration of the M^{2+} ion, systematic trends can be observed in the behavior of calcite-group minerals. The frequencies of all bands decrease with increasing unit cell volume (Figure 10a,d,g). However, the external translational and $2\nu_2$ overtone modes respond to pressure in the opposite way to external librational and internal ν_4, ν_1, and ν_3 modes. The pressure-induced shift of the external translational and $2\nu_2$ overtone bands decreases with increasing unit cell volume and compressibility (Figure 10b,c), while the pressure-induced shift of the external librational and internal ν_4, ν_1, and ν_3 bands increases with increasing unit cell volume and compressibility (Figure 10e,f,h,i). These contrasting trends can be explained by the differences in displacement vectors of atoms associated with these vibrations. For the external translational and ν_2 bands this displacement has a significantly larger component parallel to *z* axis (Caracas and Bobocioiu 2011). The opposite trends in pressure induced behavior of the two external modes become apparent when plotting their pressure-induced shifts against each other (Figure 11a). When considering calcite-group carbonates with M^{2+} ions of different kinds separately, clear correlations between the pressure-induced frequency shifts of external L band and axial compressibility along *x* crystallographic axis can be seen (Figure 11b). These trends limited to subgroups of carbonates with cations of similar configuration suggest that besides size, differences in electronegativity and bonding type are important controls on the pressure response of carbonates. Whereas bonds between alkali earth metals (having low electronegativity, Table 1) and oxygen are strongly ionic, those between transition metals (having moderate electronegativity, Table 1) often possess some covalent character. Understanding the exact mechanism underlying high-pressure vibrational and structural behavior requires quantitative data on electron density distribution in different carbonates (Zhang and Reeder 1999). Similarly to aragonite-group carbonate minerals, those

Always consult and cite the final, published document. See http:/www.minsocam.org or GeoscienceWorld

belonging to the calcite group show no systematic trends between the thermal expansion coefficient and unit cell volume or the temperature-induced shift of any band and unit cell volume. The only moderate correlation can be seen between the temperature-induced shift of the external T and L bands possibly indicating an opposite response of these bands to temperature (Figure 11c).

An additional enigmatic feature is the pressure response of the most intense internal ν_1 symmetric C–O stretching mode in aragonite versus calcite-group carbonate minerals. The pressure-induced shift decreases with increasing unit cell volume and compressibility in aragonite -group carbonate minerals, while it increases with increasing unit cell volume and compressibility in calcite-group carbonates.

Anharmonic contribution to thermodynamic properties

The anharmonicity of vibrational modes has considerable effect on the thermodynamic properties of these phases at high-temperature conditions. The anharmonic parameter can be used for the correction and calculation of numerous thermodynamic properties, including the thermal contributions to the internal energy, the isochoric heat capacity, which is responsible for the departure from the Dulong-Petit limit at high temperature, the isobaric heat capacity, and the thermal contribution to the entropy (Gillet et al. 1989; Gillet 1996; Matas et al. 2000; Oganov and Dorogokupets 2004).

Harmonic expressions for the thermal contributions to the internal energy, ε_T-ε_0, isochoric (constant-volume) specific heat, C_V, isobaric (constant-pressure) specific heat, C_P, and thermal contribution to the entropy, S_T-S_0, are (Erba et al. 2015; Wang et al. 2019b):

Always consult and cite the final, published document. See http:/www.minsocam.org or GeoscienceWorld

$$\varepsilon_T - \varepsilon_0 = \sum_{i=1}^{3N} h\nu_i \left(\frac{1}{2} + \frac{1}{e^{\frac{h\nu_i}{kT}} - 1} \right)$$

$$C_V = \sum_{i=1}^{3N} \left(\frac{(h\nu_i)^2}{kT^2} \frac{e^{\frac{h\nu_i}{kT}}}{\left(e^{\frac{h\nu_i}{kT}} - 1\right)^2} \right)$$

$$C_P = C_V + \alpha^2 K_T K V_T T$$

$$S_T - S_0 = \int_0^T \frac{C_P}{T} dT$$

where k is the Boltzmann constant, h is Planck's constant, and V_T is the equilibrium volume at temperature T.

The anharmonic corrections for the internal energy and isochoric specific heat are given by (Gillet et al. 1989; Matas et al. 2000):

$$\varepsilon(anh) = \varepsilon(1 - a_i T)$$

$$C_V(anh) = C_V(1 - a_i T)$$

The measurement of frequencies and anharmonic parameters of individual vibrational modes therefore allows a robust evaluation of importance of any anharmonic thermodynamic properties. The availability of such data is limited to the geologically most relevant carbonate phases only, namely calcite, dolomite, and magnesite (Wang et al. 2019b). Thermodynamic properties for these three phases calculated based on the harmonic and anharmonic approximation and the difference between the two are reported in Figure 12. We find that anharmonic effects are most pronounced for calcite, whereas the properties of magnesite are influenced the least, in agreement with earlier reports (Wang et al. 2019b). Values for the thermal contribution to the internal energy are comparable to those reported previously (Wang et al. 2019b). Small differences arise from the use of recently measured values of frequency and anharmonic

Always consult and cite the final, published document. See http:/www.minsocam.org or GeoscienceWorld

This is the peer-reviewed, final accepted version for American Mineralogist, published by the Mineralogical Society of America.
The published version is subject to change. Cite as Authors (Year) Title. American Mineralogist, in press.
DOI: https://doi.org/10.2138/am-2020-7404. http://www.minsocam.org/

parameters of Raman-active modes (Farsang et al. 2018). Anharmonic corrections for other thermodynamic properties differ approximately by a factor of two. This is due to the fact that Wang et al. (2019b) adopted the widely used incorrect factor of $2a_iT$ rather than a_iT to calculate the anharmonic contribution to thermodynamic properties (Matas et al. 2000).

Implications

At ambient pressure, the stability (in air) of many of the studied carbonate minerals approaches or even extends beyond 500 ˚C. At high-pressure, their stability likely increases to even higher temperatures and carbonates may serve as potential reservoirs for a number of metals (e.g., Co, Ni, Zn, Cd) in a range of crustal and upper mantle environments (e.g., subduction zones). Further experiments are needed to test the simultaneous high-pressure and high-temperature stability of these carbonate phases, including their solubility behavior in aqueous fluids resembling those present in subduction zones.

A significant anharmonic contribution to thermodynamic properties has been demonstrated for calcite, magnesite, and dolomite. To quantify these properties for the remaining carbonates, complimentary spectroscopic experiments addressing the high-pressure and high-temperature vibrational behavior of their acoustic and IR-active modes are necessary. The calculated anharmonic thermodynamic properties allow the refinement of phase equilibria at high-pressure and high-temperature conditions and should be implemented in any calculation addressing phase behavior in high-temperature environments. This is necessary for understanding a range of subduction zone geologic processes involving carbonate minerals (e.g., devolatilization, melting, dissolution in slab fluids) and modeling the deep carbon cycle.

Always consult and cite the final, published document. See http:/www.minsocam.org or GeoscienceWorld

This is the peer-reviewed, final accepted version for American Mineralogist, published by the Mineralogical Society of America.
The published version is subject to change. Cite as Authors (Year) Title. American Mineralogist, in press.
DOI: https://doi.org/10.2138/am-2020-7404. http://www.minsocam.org/

Isotope fractionation is also controlled by the thermodynamic properties (e.g., Gibbs free energy) of respective phases. Thermodynamic properties corrected for anharmonicity should therefore be used for calculating isotope fractionation factors at the high-pressure and high-temperature environments of deep Earth (Gillet et al. 1996; Polyakov 1998).

Acknowledgements

Robin Hansen and Michael S. Rumsey of the Natural History Museum, London, UK are acknowledged for the carbonate mineral samples. We thank Giulio I. Lampronti and Iris Buisman for their assistance with XRD and EPMA analysis, respectively. Xiang Wang and Yu Ye are acknowledged for providing their calculations. This work was supported by the Natural Environment Research Council (grant numbers NE/L002507/1 and NE/P019714/1).

Always consult and cite the final, published document. See http:/www.minsocam.org or GeoscienceWorld

This is the peer-reviewed, final accepted version for American Mineralogist, published by the Mineralogical Society of America.
The published version is subject to change. Cite as Authors (Year) Title. American Mineralogist, in press.
DOI: https://doi.org/10.2138/am-2020-7404. http://www.minsocam.org/

References cited

Ague, J.J., and Nicolescu, S. (2014) Carbon dioxide released from subduction zones by fluid-mediated reactions. Nature Geoscience, 7, 355–360.

Antao, S.M., and Hassan, I. (2010) Temperature dependence of the structural parameters in the transformation of aragonite to calcite, as determined from in situ synchrotron powder X-ray-diffraction data. The Canadian Mineralogist, 48, 1225–1236.

Ballirano, P. (2016) Thermal behaviour of otavite, $CdCO_3$. European Journal of Mineralogy, 28, 285–293.

Bayarjargal, L., Fruhner, C.-J., Schrodt, N., and Winkler, B. (2018) $CaCO_3$ phase diagram studied with Raman spectroscopy at pressures up to 50 GPa and high temperatures and DFT modeling. Physics of the Earth and Planetary Interiors, 281, 31–45.

Bénézeth, P., Dandurand, J.L., and Harrichoury, J.C. (2009) Solubility product of siderite ($FeCO_3$) as a function of temperature (25-250 °C). Chemical Geology, 265, 3–12.

Biedermann, N., Speziale, S., Winkler, B., Reichmann, H.J., Koch-Müller, M., and Heide, G. (2017a) High-pressure phase behavior of $SrCO_3$: an experimental and computational Raman scattering study. Physics and Chemistry of Minerals, 44, 335–343.

Biedermann, N., Winkler, B., Speziale, S., Reichmann, H.J., and Koch-Müller, M. (2017b) Single-crystal elasticity of $SrCO_3$ by Brillouin spectroscopy. High Pressure Research, 37, 181–192.

Biellmann, C., and Gillet, P. (1992) High-pressure and high-temperature behaviour of calcite, aragonite and dolomite: a Raman spectroscopic study. European Journal of Mineralogy, 4, 389–393.

Bischoff, W.D., Sharma, S.K., and Mackenzie, F.T. (1985) Carbonate ion disorder in synthetic and biogenic magnesian calcites: a Raman spectral study. American Mineralogist, 70, 581–589.

Bissengaliyeva, M.R., Gogol, D.B., Taimassova, S.T., and Bekturganov, N.S. (2012) The heat capacity and thermodynamic functions of cerussite. Journal of Chemical Thermodynamics, 47, 197–202.

Born, M., and Huang, K. (1954) Dynamical theory of crystal lattices. Clarendon press.

Borodina, U., Likhacheva, A., Golovin, A., Goryainov, S., Rashchenko, S., and Korsakov, A. (2018) Raman spectra of shortite $Na_2Ca_2(CO_3)_3$ compressed up to 8 GPa. High Pressure Research, 38, 293–302.

Boulard, E., Goncharov, A.F., Blanchard, M., and Mao, W.L. (2015) Pressure-induced phase transition in $MnCO_3$ and its implications on the deep carbon cycle. Journal of Geophysical Research: Solid Earth, 120, 4069–4079.

Brehat, F., and Wyncke, B. (1985) Analysis of the temperature-dependent infrared active lattice

Always consult and cite the final, published document. See http:/www.minsocam.org or GeoscienceWorld

This is the peer-reviewed, final accepted version for American Mineralogist, published by the Mineralogical Society of America.
The published version is subject to change. Cite as Authors (Year) Title. American Mineralogist, in press.
DOI: https://doi.org/10.2138/am-2020-7404. http://www.minsocam.org/

modes in the ordered phase of sodium nitrate. Journal of Physics C: Solid State Physics, 18, 4247–4259.

Bridgman, P.W. (1938) The high pressure behavior of miscellaneous minerals. American Journal of Science, 237, 7–18.

Caracas, R., and Bobocioiu, E. (2011) The WURM project—a freely available web-based repository of computed physical data for minerals. American Mineralogist, 96, 437–443.

Carteret, C., De La Pierre, M., Dossot, M., Pascale, F., Erba, A., and Dovesi, R. (2013) The vibrational spectrum of $CaCO_3$ aragonite: A combined experimental and quantum-mechanical investigation. The Journal of Chemical Physics, 138.

Cerantola, V., McCammon, C., Kupenko, I., Kantor, I., Marini, C., Wilke, M., Ismailova, L., Solopova, N., Chumakov, A., Pascarelli, S., and others (2015) High-pressure spectroscopic study of siderite ($FeCO_3$) with a focus on spin crossover. American Mineralogist, 100, 2670–2681.

Chaney, J., Santillán, J.D., Knittle, E., and Williams, Q. (2015) A high-pressure infrared and Raman spectroscopic study of $BaCO_3$: the aragonite, trigonal and Pmmn structures. Physics and Chemistry of Minerals, 42, 83–93.

Chariton, S., Cerantola, V., Ismailova, L., Bykova, E., Bykov, M., Kupenko, I., McCammon, C., and Dubrovinsky, L. (2018) The high-pressure behavior of spherocobaltite ($CoCO_3$): a single crystal Raman spectroscopy and XRD study. Physics and Chemistry of Minerals, 45, 59–68.

Chen, C.-C., Lin, C.-C., Liu, L.-G., Sinogeikin, S. V., and Bass, J.D. (2001) Elasticity of single-crystal calcite and rhodochrosite by Brillouin spectroscopy. American Mineralogist, 86, 1525–1529.

Cloots, R. (1991) Raman spectrum of carbonates $M^{II}CO_3$ in the 1100-1000 cm^{-1} region: observation of the n_1 mode of the isotopic $(C^{16}O_2{}^{18}O)^{2-}$ ion. Spectrochimica Acta, 47A, 1745–1750.

Cortez-Valadez, M., Vargas-Ortiz, A., Rojas-Blanco, L., Arizpe-Chávez, H., Flores-Acosta, M., and Ramírez-Bon, R. (2013) Additional active Raman modes in α-PbO nanoplates. Physica E: Low-Dimensional Systems and Nanostructures, 53, 146–149.

Couture, L. (1947) Étude des spectres de vibrations de monocristaux ioniques. In Annales de physique Vol. 12, pp. 5–94. EDP Sciences.

Dasgupta, R., and Hirschmann, M.M. (2010) The deep carbon cycle and melting in Earth's interior. Earth and Planetary Science Letters, 298, 1–13.

De La Pierre, M., Carteret, C., Maschio, L., André, E., Orlando, R., and Dovesi, R. (2014) The Raman spectrum of $CaCO_3$ polymorphs calcite and aragonite: A combined experimental and computational study. The Journal of Chemical Physics, 140, 164509.

Decremps, F., Pellicer-Porres, J., Saitta, A.M., Chervin, J.-C., and Polian, A. (2002) High-

Always consult and cite the final, published document. See http:/www.minsocam.org or GeoscienceWorld

This is the peer-reviewed, final accepted version for American Mineralogist, published by the Mineralogical Society of America.
The published version is subject to change. Cite as Authors (Year) Title. American Mineralogist, in press.
DOI: https://doi.org/10.2138/am-2020-7404. http://www.minsocam.org/

pressure Raman spectroscopy study of wurtzite ZnO. Physical Review B: Condensed Matter and Materials Physics, 65, 92101.

Dietz, R.E., Parisot, G.I., and Meixner, A.E. (1971) Infrared absorption and Raman scattering by two-magnon processes in NiO. Physical Review B, 4, 2302–2310.

Dufresne, W.J.B., Rufledt, C.J., and Marshall, C.P. (2018) Raman spectroscopy of the eight natural carbonate minerals of calcite structure. Journal of Raman Spectroscopy, 1–9.

Efthimiopoulos, I., Jahn, S., Kuras, A., Schade, U., and Koch-Müller, M. (2017) Combined high-pressure and high-temperature vibrational studies of dolomite: phase diagram and evidence of a new distorted modification. Physics and Chemistry of Minerals, 44, 465–476.

Efthimiopoulos, I., Germer, M., Jahn, S., Harms, M., Reichmann, H.J., Speziale, S., Schade, U., Sieber, M., and Koch-Müller, M. (2018) Effects of hydrostaticity on the structural stability of carbonates at lower mantle pressures: the case study of dolomite. High Pressure Research, 39, 36–49.

Efthimiopoulos, I., Müller, J., Winkler, B., Otzen, C., Harms, M., Schade, U., and Koch-Müller, M. (2019) Vibrational response of strontianite at high pressures and high temperatures and construction of P–T phase diagram. Physics and Chemistry of Minerals, 46, 27–35.

Erba, A., Shahrokhi, M., Moradian, R., and Dovesi, R. (2015) On how differently the quasi-harmonic approximation works for two isostructural crystals: Thermal properties of periclase and lime. Journal of Chemical Physics, 142.

Farfan, G., Wang, S., Ma, H., Caracas, R., and Mao, W.L. (2012) Bonding and structural changes in siderite at high pressure. American Mineralogist, 97, 1421–1426.

Farfan, G.A., Boulard, E., Wang, S., and Mao, W.L. (2013) Bonding and electronic changes in rhodochrosite at high pressure. American Mineralogist, 98, 1817–1823.

Farsang, S., Facq, S., and Redfern, S.A.T. (2018) Raman modes of carbonate minerals as pressure and temperature gauges up to 6 GPa and 500 °C. American Mineralogist, 103, 1988–1998.

Fong, M.Y., and Nicol, M. (1971) Raman spectrum of calcium carbonate at high pressures. The Journal of Chemical Physics, 54, 579–585.

Gao, J., and Yuan, X. (2020) Vibrational investigation of pressure-induced phase transitions of hydroxycarbonate malachite $Cu_2(CO_3)(OH)_2$. Minerals, 10, 277.

Gao, J., Zhu, F., Lai, X.-J., Huang, R., Qin, S., Chen, D.-L., Liu, J., Zheng, L.-R., and Wu, X. (2014) Compressibility of a natural smithsonite $ZnCO_3$ up to 50 GPa. High Pressure Research, 34, 89–99.

Gao, J., Wu, X., Qin, S., and Li, Y.-C. (2016) Pressure-induced phase transformations of $PbCO_3$ by X-ray diffraction and Raman spectroscopy. High Pressure Research, 36, 1–15.

Gavryushkin, P.N., Martirosyan, N.S., Inerbaev, T.M., Popov, Z.I., Rashchenko, S. V.,

Always consult and cite the final, published document. See http:/www.minsocam.org or GeoscienceWorld

This is the peer-reviewed, final accepted version for American Mineralogist, published by the Mineralogical Society of America.
The published version is subject to change. Cite as Authors (Year) Title. American Mineralogist, in press.
DOI: https://doi.org/10.2138/am-2020-7404. http://www.minsocam.org/

Likhacheva, A.Y., Lobanov, S.S., Goncharov, A.F., Prakapenka, V.B., and Litasov, K.D. (2017) Aragonite-II and $CaCO_3$-VII: New high-pressure, high-temperature polymorphs of $CaCO_3$. Crystal Growth & Design, 17, 6291–6296.

Gervais, F., Piriou, B., and Cabannes, F. (1973) Anharmonicity in silicate crystals: Temperature dependence of Au type vibrational modes in $ZrSiO_4$ and $LiAlSi_2O_6$. Journal of Physics and Chemistry of Solids, 34, 1785–1796.

Gillet, P. (1993) Stability of magnesite ($MgCO_3$) at mantle pressure and temperature conditions: A Raman spectroscopic study. American Mineralogist, 78, 1328–1331.

Gillet, P. (1996) Raman spectroscopy at high pressure and high temperature. Phase transitions and thermodynamic properties of minerals. Physics and Chemistry of Minerals, 23, 263–275.

Gillet, P., Guyot, F., and Malezieux, J.M. (1989) High-pressure, high-temperature Raman spectroscopy of Ca_2GeO_4 (olivine form): some insights on anharmonicity. Physics of the Earth and Planetary Interiors, 58, 141–154.

Gillet, P., Biellmann, C., Reynard, B., and McMillan, P. (1993) Raman spectroscopic studies of carbonates Part I: High-pressure and high-temperature behaviour of calcite, magnesite, dolomite and aragonite. Physics and Chemistry of Minerals, 20, 1–18.

Gillet, P., Mcmillan, P., Schott, J., Badro, J., and Grzechnik, A. (1996) Thermodynamic properties and isotopic fractionation of calcite from vibrational spectroscopy of 18O-substituted calcite. Geochimica et Cosmochimica Acta, 60, 3471–3485.

Gillet, P., Hemley, R.J., and McMillan, P.F. (1998) Vibrational properties at high pressures and temperatures. Ultrahigh-pressure mineralogy, 525–590.

Graf, D.L. (1961) Crystallographic tables for the rhombohedral carbonates. American Mineralogist, 46, 1283–1316.

Greenaway, A.M., Dasgupta, T.P., Koshy, K.C., and Sadler, G.G. (1986) A correlation between infrared stretching mode absorptions and structural angular distortions for the carbonato ligand in a wide variety of complexes. Spectrochimica Acta Part A: Molecular Spectroscopy, 42, 949–954.

Gurevich, V.M., Gavrichev, K.S., Gorbunov, V.E., Danilova, T. V, and Golushina, L.N. (2001a) Low-temperature heat capacity of strontianite $SrCO_3$(c). Geochem International, 39, 676–682.

——— (2001b) Low-temperature heat capacity of witherite $BaCO_3$(c). Geochem International, 39, 1007–1014.

Hales, M.C., and Frost, R.L. (2008) Thermal analysis of smithsonite and hydrozincite. Journal of Thermal Analysis and Calorimetry, 91, 855–860.

Haselton, H.T., and Goldsmith, J.R. (1987) The decarbonation and heat capacity of $ZnCO_3$. Geochimica et Cosmochimica Acta, 51, 261–265.

Always consult and cite the final, published document. See http:/www.minsocam.org or GeoscienceWorld

Haynes, W.M. (2016) CRC Handbook of Chemistry and Physics. CRC Press, Boca Raton, Florida.

Hemingway, B.S., Robie, R.A., Fisher, J.R., and Wilson, W.H. (1977) Heat capacities of gibbsite, $Al(OH)_3$, between 13 and 480 K and magnesite, $MgCO_3$, between 13 and 380 K and their standard entropies at 289.15 K, and the heat capacities of calorimetry conference benzoic acid benween 12 and 316 K. Journal of Research of the US Geological Survey, 5, 797–806.

Herman, R.G., Bogdan, C.E., Sommer, A.J., and Simpson, D.R. (1987) Discrimination among carbonate minerals by Raman spectroscopy using the laser microprobe. Applied Spectroscopy, 41, 437–440.

Hess, N.J., Exarhos, G.J., and Ghose, S. (1991) Raman spectroscopy at simultaneous pressure and temperature: Phase relations and lattice dynamics of $CaCO_3$.

Humbert, P., and Plicque, F. (1972) Propriétés élastiques des carbonates rhombohédriques monocristallins: calcite, magnésite et dolomie. Comptes Rendus de l'Académie des Sciences de Paris, 275, 391–394.

Kelemen, P.B., and Manning, C.E. (2015) Reevaluating carbon fluxes in subduction zones, what goes down, mostly comes up. Proceedings of the National Academy of Sciences, 112, E3997–E4006.

Klotz, S., Chervin, J.-C., Munsch, P., and Le Marchand, G. (2009) Hydrostatic limits of 11 pressure transmitting media. Journal of Physics D: Applied Physics, 42, 075413.

Koch-Müller, M., Jahn, S., Birkholz, N., Ritter, E., and Schade, U. (2016) Phase transitions in the system $CaCO_3$ at high P and T determined by in situ vibrational spectroscopy in diamond anvil cells and first-principles simulations. Physics and Chemistry of Minerals, 43, 545–561.

Kraft, S., Knittle, E., and Williams, Q. (1991) Carbonate stability in the Earth's mantle: A vibrational spectroscopic study of aragonite and dolomite at high pressures and temperatures. Journal of Geophysical Research, 96, 17997–18009.

Krishnamurti, D. (1956) Raman spectrum of magnesite. Proceedings of the Indian Academy of Sciences - Section A, 43, 210–212.

Krishnamurti, D. (1957) The Raman spectrum of calcite and its interpretation. Proceedings of the Indian Academy of Sciences - Section A, 44, 183–202.

Krishnan, R.S. (1945) Raman spectra of the second order in crystals Part I: Calcite. Proceedings of the Indian Academy of Sciences - Section A, 182–192.

Letoullec, R., Pinceaux, J.P., and Loubeyre, P. (1988) The membrane diamond anvil cell: A new device for generating continuous pressure and temperature variations. High Pressure Research, 1, 77–90.

Li, Y., Zou, Y., Chen, T., Wang, X., Qi, X., Chen, H., Du, J., and Li, B. (2015) P-V-T equation

Always consult and cite the final, published document. See http:/www.minsocam.org or GeoscienceWorld

This is the peer-reviewed, final accepted version for American Mineralogist, published by the Mineralogical Society of America.
The published version is subject to change. Cite as Authors (Year) Title. American Mineralogist, in press.
DOI: https://doi.org/10.2138/am-2020-7404. http://www.minsocam.org/

of state and high-pressure behavior of $CaCO_3$ aragonite. American Mineralogist, 100, 2323–2329.

Liang, W., Li, Z., Yin, Y., Li, R., Chen, L., He, Y., Dong, H., Dai, L., and Li, H. (2018a) Single crystal growth, characterization and high-pressure Raman spectroscopy of impurity-free magnesite ($MgCO_3$). Physics and Chemistry of Minerals, 45, 423–434.

Liang, W., Yin, Y., Li, Zeming, Li, R., Li, L., He, Y., Dong, H., Li, Zengsheng, Yan, S., Zhai, S., and others (2018b) Single crystal growth, crystalline structure investigation and high-pressure behavior of impurity-free siderite ($FeCO_3$). Physics and Chemistry of Minerals, 45, 831–842.

Lin, C.-C., and Liu, L.-G. (1997a) High-pressure Raman spectroscopic study of post-aragonite phase transition in witherite ($BaCO_3$). European Journal of Mineralogy, 9, 785–792.

——— (1997b) High pressure phase transformations in aragonite-type carbonates. Physics and Chemistry of Minerals, 24, 149–157.

——— (1997c) Post-aragonite phase transitions in strontianite and cerussite—A high-pressure Raman spectroscopic study. Journal of Physics and Chemistry of Solids, 58, 977–987.

Lin, J.-F., Liu, J., Jacobs, C., and Prakapenka, V.B. (2012) Vibrational and elastic properties of ferromagnesite across the electronic spin-pairing transition of iron. American Mineralogist, 97, 583–591.

Litasov, K.D., Shatskiy, A., Gavryushkin, P.N., Bekhtenova, A.E., Dorogokupets, P.I., Danilov, B.S., Higo, Y., Akilbekov, A.T., and Inerbaev, T.M. (2017) P-V-T equation of state of $CaCO_3$ aragonite to 29 GPa and 1673 K: In situ X-ray diffraction study. Physics of the Earth and Planetary Interiors, 265, 82–91.

Liu, C., Zheng, H., and Wang, D. (2017) Raman spectroscopic study of calcite III to aragonite transformation under high pressure and high temperature. High Pressure Research, 37, 545–557.

Liu, J., Caracas, R., Fan, D., Bobocioiu, E., Zhang, D., and Mao, W.L. (2016) High-pressure compressibility and vibrational properties of $(Ca,Mn)CO_3$. American Mineralogist, 101, 2723–2730.

Liu, L.-G., and Mernagh, T.P. (1990) Phase transitions and Raman spectra of calcite at high pressures and room temperature. American Mineralogist, 75, 801–806.

Liu, L.-G., Chen, C., Lin, C.-C., and Yang, Y. (2005) Elasticity of single-crystal aragonite by Brillouin spectroscopy. Physics and Chemistry of Minerals, 32, 97–102.

Lobanov, S.S., Dong, X., Martirosyan, N.S., Samtsevich, A.I., Stevanovic, V., Gavryushkin, P.N., Litasov, K.D., Greenberg, E., Prakapenka, V.B., Oganov, A.R., and others (2017) Raman spectroscopy and x-ray diffraction of sp^3 $CaCO_3$ at lower mantle pressures. Physical Review B, 96, 104101.

Manning, C.E. (2014) A piece of the deep carbon puzzle. Nature Geoscience, 7, 333–334.

Always consult and cite the final, published document. See http:/www.minsocam.org or GeoscienceWorld

This is the peer-reviewed, final accepted version for American Mineralogist, published by the Mineralogical Society of America.
The published version is subject to change. Cite as Authors (Year) Title. American Mineralogist, in press.
DOI: https://doi.org/10.2138/am-2020-7404. http://www.minsocam.org/

Mao, H.K., Xu, J., and Bell, P.M. (1986) Calibration of the ruby pressure gauge to 800 kbar under quasi-hydrostatic conditions. Journal of Geophysical Research, 91, 4673–4676.

Markgraf, S.A., and Reeder, R.J. (1985) High-temperature structure refinements of calcite and magnesite. American Mineralogist, 70, 590–600.

Martens, W.N., Rintoul, L., Kloprogge, J.T., and Frost, R.L. (2004) Single crystal raman spectroscopy of cerussite. American Mineralogist, 89, 352–358.

Martinez, I., Zhang, J., and Reeder, R.J. (1996) In situ X-ray diffraction of aragonite and dolomite at high pressure and high temperature: Evidence for dolomite breakdown to aragonite and magnesite. American Mineralogist, 81, 611–624.

Maruyama, K., Kagi, H., Komatsu, K., Yoshino, T., and Nakano, S. (2017) Pressure-induced phase transitions of vaterite, a metastable phase of $CaCO_3$. Journal of Raman Spectroscopy, 48, 1449–1453.

Matas, J., Gillet, P., Ricard, Y., and Martinez, I. (2000) Thermodynamic properties of carbonates at high pressures from vibrational modelling. European Journal of Mineralogy, 12, 703–720.

Megaw, H.D. (1970) Thermal vibrations and a lattice mode in calcite and sodium nitrate. Acta Crystallographica Section A, 26, 235–244.

Minch, R., Seoung, D.-H., Ehm, L., Winkler, B., Knorr, K., Peters, L., Borkowski, L.A., Parise, J.B., Lee, Y., Dubrovinsky, L., and others (2010a) High-pressure behavior of otavite ($CdCO_3$). Journal of Alloys and Compounds, 508, 251–257.

Minch, R., Dubrovinsky, L., Kurnosov, A., Ehm, L., Knorr, K., and Depmeier, W. (2010b) Raman spectroscopic study of $PbCO_3$ at high pressures and temperatures. Physics and Chemistry of Minerals, 37, 45–56.

Müller, J., Speziale, S., Efthimiopoulos, I., Jahn, S., and Koch-Müller, M. (2016) Raman spectroscopy of siderite at high pressure: Evidence for a sharp spin transition. American Mineralogist, 101, 2638–2644.

Müller, J., Efthimiopoulos, I., Jahn, S., and Koch-Müller, M. (2017) Effect of temperature on the pressure-induced spin transition in siderite and iron-bearing magnesite: a Raman spectroscopy study. European Journal of Mineralogy, 29, 785–793.

Nicol, M., and Ellenson, W.D. (1972) Raman spectrum of $CaCO_3$III at 77 K. The Journal of Chemical Physics, 56, 677–678.

Oganov, A.R., and Dorogokupets, P.I. (2004) Intrinsic anharmonicity in equations of state and thermodynamics of solids. Journal of Physics Condensed Matter, 16, 1351–1360.

Peercy, P.S., and Morosin, B. (1973) Pressure and temperature dependences of the Raman-active phonons in SnO_2. Physical Review B, 7, 2779–2786.

Picard, A., Oger, P.M., Daniel, I., Cardon, H., Montagnac, G., and Chervin, J.-C. (2006) A

Always consult and cite the final, published document. See http:/www.minsocam.org or GeoscienceWorld

This is the peer-reviewed, final accepted version for American Mineralogist, published by the Mineralogical Society of America.
The published version is subject to change. Cite as Authors (Year) Title. American Mineralogist, in press.
DOI: https://doi.org/10.2138/am-2020-7404. http://www.minsocam.org/

sensitive pressure sensor for diamond anvil cell experiments up to 2 GPa: FluoSpheres®. Journal of Applied Physics, 100, 034915.

Pippinger, T., Miletich, R., Merlini, M., Lotti, P., Schouwink, P., Yagi, T., Crichton, W.A., and Hanfland, M. (2015) Puzzling calcite-III dimorphism: crystallography, high-pressure behavior, and pathway of single-crystal transitions. Physics and Chemistry of Minerals, 42, 29–43.

Plank, T., and Manning, C.E. (2019) Subducting carbon. Nature, 574, 343–352.

Polyakov, V.B. (1998) On anharmonic and pressure corrections to the equilibrium isotopic constants for minerals. Geochimica et Cosmochimica Acta, 62, 3077–3085.

Popkov, Y.A., Eremenko, V. V., Fomin, V.I., and Mokhir, A.P. (1972) Kombinacionnoe rasseyanie sveta v antiferromagnitnom siderite (Raman light scattering in antiferromagnetic siderite). Fizika Tverdogo Tela (Solid State Pysics), 14, 2294–2299.

Rashchenko, S. V., Goryainov, S. V., Romanenko, A. V., Golovin, A. V., Korsakov, A. V., Moine, B.N., and Mikhno, A.O. (2017) High-pressure Raman study of nyerereite from Oldoinyo Lengai. Journal of Raman Spectroscopy, 48, 1438–1442.

Redfern, S.A.T. (2000) Structural variations in carbonates. Reviews in Mineralogy and Geochemistry, 41, 289–308.

Redfern, S.A.T., and Angel, R.J. (1999) High-pressure behaviour and equation of state of calcite, $CaCO_3$. Contributions to Mineralogy and Petrology, 134, 102–106.

Redfern, S.A.T., Salje, E., and Navrotsky, A. (1989) High-temperature enthalpy at the orientational order-disorder transition in calcite: implications for the calcite/aragonite phase equilibrium. Contributions to Mineralogy and Petrology, 101, 479–484.

Redfern, S.A.T., Wood, B.J., and Henderson, C.M.B. (1993) Static compressibility of magnesite to 20 GPa: Implications for $MgCO_3$ in the lower mantle. Geophysical Research Letters, 20, 2099–2102.

Reeder, R.J., and Markgraf, S.A. (1986) High-temperature crystal chemistry of dolomite. American Mineralogist, 71, 795–804.

Robie, R.A., Haselton, H.T., and Hemingway, B.S. (1984) Heat capacities and entropies of rhodochrosite ($MnCO_3$) and siderite ($FeCO_3$) between 5 and 600 K. American Mineralogist, 69, 349–357.

Ross, N.L., and Reeder, R.J. (1992) High-pressure structural study of dolomite and ankerite. American Mineralogist, 77, 412–421.

Rutt, H.N., and Nicola, J.H. (1974) Raman spectra of carbonates of calcite structure. Journal of Physics C: Solid State Physics, 7, 4522–4528.

Salje, E., and Viswanathan, K. (1976) The phase diagram calcite-aragonite as derived from the crystallographic properties. Contributions to Mineralogy and Petrology, 55, 55–67.

Always consult and cite the final, published document. See http:/www.minsocam.org or GeoscienceWorld

This is the peer-reviewed, final accepted version for American Mineralogist, published by the Mineralogical Society of America.
The published version is subject to change. Cite as Authors (Year) Title. American Mineralogist, in press.
DOI: https://doi.org/10.2138/am-2020-7404. http://www.minsocam.org/

Saloman, E.B., and Sansonetti, C.J. (2004) Wavelengths, energy level classifications, and energy levels for the spectrum of neutral neon. Journal of Physical and Chemical Reference Data, 33, 1113–1158.

Sanchez-Valle, C., Ghosh, S., and Rosa, A.D. (2011) Sound velocities of ferromagnesian carbonates and the seismic detection of carbonates in eclogites and the mantle. Geophysical Research Letters, 38, L24315.

Santillán, J., and Williams, Q. (2004) A high-pressure infrared and X-ray study of $FeCO_3$ and $MnCO_3$: Comparison with $CaMg(CO_3)_2$-dolomite. Physics of the Earth and Planetary Interiors, 143–144, 291–304.

Shahar, A., Bassett, W.A., Mao, H.-K., Chou, I.-M., and Mao, W. (2005) The stability and Raman spectra of ikaite, $CaCO_3 \cdot 6H_2O$, at high pressure and temperature. American Mineralogist, 90, 1835–1839.

Shannon, R.D. (1976) Revised effective ionic radii and systematic studies of interatomic distances in halides and chalcogenides. Acta Crystallographica Section A, 32, 751–767.

Shi, W., Fleet, M.E., and Shieh, S.R. (2012) High-pressure phase transitions in Ca-Mn carbonates $(Ca,Mn)CO_3$ studied by Raman spectroscopy. American Mineralogist, 97, 999–1001.

Spivak, A., Solopova, N., Cerantola, V., Bykova, E., Zakharchenko, E., Dubrovinsky, L., and Litvin, Y. (2014) Raman study of $MgCO_3$-$FeCO_3$ carbonate solid solution at high pressures up to 55 GPa. Physics and Chemistry of Minerals, 41, 633–638.

Staveley, L.A.K., and Linford, R.G. (1969) The heat capacity and entropy of calcite and aragonite, and their interpretation. The Journal of Chemical Thermodynamics, 1, 1–11.

Stout, J., and Robie, R. (1963) Heat capacity from 11 to 300˚K., entropy, and heat of formation of dolomite. The Journal of Physical Chemistry, 67, 2248–2252.

Suito, K., Namba, J., Horikawa, T., Taniguchi, Y., Sakurai, N., Kobayashi, M., Onodera, A., Shimomura, O., and Kikegawa, T. (2001) Phase relations of $CaCO_3$ at high pressure and high temperature. American Mineralogist, 86, 997–1002.

Ungureanu, C.G., Prencipe, M., and Cossio, R. (2010) Ab initio quantum-mechanical calculation of $CaCO_3$ aragonite at high pressure: thermodynamic properties and comparison with experimental data. European Journal of Mineralogy, 22, 693–701.

Vennari, C.E., and Williams, Q. (2018) A novel carbon bonding environment in deep mantle high-pressure dolomite. American Mineralogist, 103, 171–174.

Vennari, C.E., Beavers, C.M., and Williams, Q. (2018) High-pressure/temperature behavior of the alkali/calcium carbonate shortite $(Na_2Ca_2(CO_3)_3)$: Implications for carbon sequestration in Earth's transition zone. Journal of Geophysical Research: Solid Earth, 123, 6574–6591.

Wagner, J.M. (2000) On the inadequacy of linear pressure dependence of vibrational frequency. Solid State Communications, 116, 355–356.

Always consult and cite the final, published document. See http:/www.minsocam.org or GeoscienceWorld

This is the peer-reviewed, final accepted version for American Mineralogist, published by the Mineralogical Society of America.
The published version is subject to change. Cite as Authors (Year) Title. American Mineralogist, in press.
DOI: https://doi.org/10.2138/am-2020-7404. http://www.minsocam.org/

Wang, M., Liu, Q., Nie, S., Li, B., Wu, Y., Gao, J., Wei, X., and Wu, X. (2015) High-pressure phase transitions and compressibilities of aragonite-structure carbonates: $SrCO_3$ and $BaCO_3$. Physics and Chemistry of Minerals, 42, 517–527.

Wang, M., Shi, G., Qin, J., and Bai, Q. (2018) Thermal behaviour of calcite-structure carbonates from a powder X-ray diffraction study between 83 and 618 K. European Journal of Mineralogy, 30, 939–949.

Wang, X., Ye, Y., Wu, X., Smyth, J.R., Yang, Y., Zhang, Z., and Wang, Z. (2019a) High-temperature Raman and FTIR study of aragonite-group carbonates. Physics and Chemistry of Minerals, 46, 51–62.

Wang, X., Xu, X., Ye, Y., Wang, C., Liu, D., Shi, X., Wang, S., and Zhu, X. (2019b) In-situ High-Temperature XRD and FTIR for Calcite, Dolomite and Magnesite: Anharmonic Contribution to the Thermodynamic Properties. Journal of Earth Science, 30, 964–976.

White, W.B. (1974) The Carbonate Minerals. In V.C. Farmer, Ed., The Infrared Spectra of Minerals pp. 227–284.

Williams, Q., Collerson, B., and Knittle, E. (1992) Vibrational spectra of magnesite ($MgCO_3$) and calcite-III at high pressures. American Mineralogist, 77, 1158–1165.

Xu, J., Kuang, Y., Zhang, B., Liu, Y., Fan, D., Zhou, W., and Xie, H. (2015) High-pressure study of azurite $Cu_3(CO_3)_2(OH)_2$ by synchrotron radiation X-ray diffraction and Raman spectroscopy. Physics and Chemistry of Minerals, 42, 805–816.

Ye, Y., Smyth, J.R., and Boni, P. (2012) Crystal structure and thermal expansion of aragonite-group carbonates by single-crystal X-ray diffraction. American Mineralogist, 97, 707–712.

Yuan, X., Gao, C., and Gao, J. (2019) An in situ study of the phase transitions among $CaCO_3$ high-pressure polymorphs. Mineralogical Magazine, 83, 191–197.

Zhang, J., and Reeder, R.J. (1999) Comparative compressibilities of calcite-structure carbonates: Deviations from empirical relations. American Mineralogist, 84, 861–870.

Zhang, J., Martinez, I., Guyot, F., and Reeder, R.J. (1998) Effects of Mg-Fe^{2+} substitution in calcite-structure carbonates: Thermoelastic properties. American Mineralogist, 83, 280–287.

Zhang, Y.-F., Liu, J., Qin, Z.-X., Lin, C.-L., Xiong, L., Li, R., and Bai, L.-G. (2013) A high-pressure study of $PbCO_3$ by XRD and Raman spectroscopy. Chinese Physics C, 37, 038001.

Zhao, C., Li, H., Jiang, J., He, Y., and Liang, W. (2018) Phase transition and vibration properties of $MnCO_3$ at high pressure and high-temperature by Raman spectroscopy. High Pressure Research, 38, 212–223.

Always consult and cite the final, published document. See http:/www.minsocam.org or GeoscienceWorld

Figure 1. Raman spectra of aragonite-group carbonate minerals aragonite, strontianite, cerussite, and witherite collected at ambient pressure (1 bar) and temperature (25 ˚C). Ionic radii are from Shannon (1976). The spectrum of aragonite is from Farsang et al. (2018). Bands marked with * are due to isotopic effects.

Figure 2. The correlation of frequencies of ν_1 internal vibrational mode with ionic radii and M–O bond lengths in aragonite-group carbonate minerals. Ionic radii are from Shannon (1976). M–O bond lengths are from Ye et al. (2012). Data for aragonite are from Farsang et al. (2018).

Figure 3a. Raman spectra of calcite-group carbonate minerals gaspeite, magnesite, smithsonite, and spherocobaltite collected at ambient pressure (1 bar) and temperature (25 ˚C). Ionic radii are from Shannon (1976). The spectrum of magnesite is from Farsang et al. (2018). The symmetry of calcite-group carbonate modes is from Rutt and Nicola (1974). Due to submicron size magnesite domains present in gaspeite, the spectrum of gaspeite contains additional bands of magnesite.

Figure 3b. Raman spectra of calcite-group carbonate siderite, rhodochrosite, otavite, and calcite collected at ambient pressure (1 bar) and temperature (25 ˚C). Ionic radii are from Shannon (1976). The spectra of siderite, rhodochrosite, and calcite are from Farsang et al. (2018). The symmetry of calcite-group carbonate modes is from Rutt and Nicola (1974).

Figure 4. The correlation of frequencies of T (a) and L (b) external vibrational modes and ν_1 (c) internal vibrational mode with ionic radii and M–O bond lengths in calcite-group carbonate minerals. Ionic radii are from Shannon (1976). M–O bond lengths are calculated by Rutt and

Always consult and cite the final, published document. See http:/www.minsocam.org or GeoscienceWorld

This is the peer-reviewed, final accepted version for American Mineralogist, published by the Mineralogical Society of America.
The published version is subject to change. Cite as Authors (Year) Title. American Mineralogist, in press.
DOI: https://doi.org/10.2138/am-2020-7404. http://www.minsocam.org/

Nicola (1974) from data of Graf (1961). Data for magnesite, siderite, rhodochrosite, and calcite are from Farsang et al. (2018).

Figure 5. Frequency evolution of the traced vibrational modes in aragonite-group carbonate minerals as a function of pressure. The experimental uncertainty lies within the size of the symbol. Ionic radii are from Shannon (1976). Data for magnesite, siderite, rhodochrosite, and calcite are from Farsang et al. (2018).

Figure 6. Frequency evolution of the traced vibrational modes in calcite-group carbonate minerals as a function of pressure. The experimental uncertainty lies within the size of the symbol. Ionic radii are from Shannon (1976). Data for magnesite, siderite, rhodochrosite, and calcite are from Farsang et al. (2018). The Fe^{2+} electronic excitation feature of siderite is not shown and can be found in Farsang et al. (2018).

Figure 7. Frequency evolution of the traced vibrational modes in aragonite-group carbonate minerals as a function of temperature. The experimental uncertainty lies within the size of the symbol. Ionic radii are from Shannon (1976). Data for magnesite, siderite, rhodochrosite, and calcite are from Farsang et al. (2018).

Figure 8. Frequency evolution of the traced vibrational modes in calcite-group carbonate minerals as a function of temperature. The experimental uncertainty lies within the size of the symbol. Ionic radii are from Shannon (1976). Data for magnesite, siderite, rhodochrosite, and calcite are from Farsang et al. (2018). The Fe^{2+} electronic excitation feature of siderite is not shown and can be found in Farsang et al. (2018).

Always consult and cite the final, published document. See http:/www.minsocam.org or GeoscienceWorld

Figure 9. a) Relationship between the frequency of the internal ν_1 band and unit cell volumes of aragonite-group carbonate minerals, b) Relationship between the pressure-induced frequency shift of ν_1 band and unit cell volumes of aragonite-group carbonate minerals, and c) Relationship between the pressure-induced frequency shift of ν_1 band and isothermal bulk moduli of aragonite group carbonate minerals. Linear correlations indicated by trend lines exist only for aragonite-group carbonate minerals having an alkaline earth element M^{2+} ion. Values of the frequency of the ν_1 band can be found in Table S3, values of unit cell parameters in Table 1, values of pressure-induced frequency shift of ν_1 band in Table S3, and values of isothermal bulk moduli in Table 5.

Figure 10. Relationships between the frequency of different bands and unit cell volumes, the pressure-induced frequency shift ($\delta\nu_i/\delta P$) and unit cell volumes, and pressure-induced frequency shift ($\delta\nu_i/\delta P$) and isothermal bulk moduli (K_T) in calcite-group carbonate minerals: a-c) external translational band, d-f) external librational band, and g-i) internal ν_1 band. Values of the frequency of different bands can be found in Table S4, values of unit cell parameters in Table 1, values of pressure-induced frequency shift of different bands in Table S4, and values of isothermal bulk moduli in Table 5.

Figure 11. a) Relationship between the pressure-induced frequency shifts ($\delta\nu_i/\delta P$) of external T and L bands, b) Relationship between the pressure-induced frequency shifts ($\delta\nu_i/\delta P$) of external L band and axial compressibility along x (β_a), and c) Relationship between the temperature-induced frequency shifts ($\delta\nu_i/\delta T$) of external T and L bands. Values of pressure and temperature-

Always consult and cite the final, published document. See http:/www.minsocam.org or GeoscienceWorld

This is the peer-reviewed, final accepted version for American Mineralogist, published by the Mineralogical Society of America.
The published version is subject to change. Cite as Authors (Year) Title. American Mineralogist, in press.
DOI: https://doi.org/10.2138/am-2020-7404. http://www.minsocam.org/

induced frequency shift of different bands can be found in Table S4 and axial compressibility values are from Zhang and Reeder (1999).

Figure 12. Thermodynamic properties as a function of temperature calculated based on the harmonic and anharmonic approximation and the difference between the two: a) thermal contribution to internal energy (ε_T-ε_0), b) isochoric heat capacity (C_V), c) isobaric heat capacity (C_P), and d) thermal contribution to entropy (S_T-S_0). Values are normalized to one mole of CO_3 groups.

Always consult and cite the final, published document. See http:/www.minsocam.org or GeoscienceWorld

Mineral	Ideal formula	Calculated formula	Ionic radius of M^{2+} (Å)	M–O bond distance (Å)	Outer electron configuration of M^{2+}	Electronegativity	Space Group	Unit cell parameters (Å)			Unit cell volume (Å^3)
								a	*b*	*c*	
Aragonite	$CaCO_3$	$Ca_{1.00}CO_3$	1.18	2.528(2)	$3s^23p^6$	1.00	*Pmcn*	4.9612(5)	7.9701(9)	5.7420(4)	227.05(4)
Cerussite	$PbCO_3$	$Pb_{0.97}Mg_{0.03}CO_3$	1.35	2.695(6)	$6s^24f^{14}5d^{10}$	1.80	*Pmcn*	5.1820(1)	8.4992(2)	6.1446(2)	270.63(1)
Strontianite	$SrCO_3$	$Sr_{0.92}Ca_{0.06}Mg_{0.01}CO_3$	1.31	2.634(9)	$4s^23d^{10}4p^6$	0.95	*Pmcn*	5.0943(2)	8.3788(4)	6.0096(3)	256.51(2)
Witherite	$BaCO_3$	$Ba_{0.98}Sr_{0.02}CO_3$	1.47	2.809(7)	$5s^24d^{10}5p^6$	0.89	*Pmcn*	5.3057(3)	8.9021(6)	6.4298(4)	303.69(3)
Calcite	$CaCO_3$	$Ca_{1.00}CO_3$	1.00	2.356	$3s^23p^6$	1.00	$R\bar{3}c$	4.9864(2)		17.0491(8)	367.13(3)
Gaspeite	$NiCO_3$	$Ni_{0.50}Mg_{0.49}Ca_{0.01}CO_3$[a]	0.69	2.071	$3d^8$	1.91	$R\bar{3}c$	4.6189(5)		14.813(2)	273.68(7)
Magnesite	$MgCO_3$	$Mg_{0.96}Ca_{0.01}Fe_{0.03}CO_3$	0.72	2.101	$2s^22p^6$	1.31	$R\bar{3}c$	4.6371(2)		15.0365(5)	280.01(2)
Otavite	$CdCO_3$	$Cd_{0.91}Zn_{0.05}Pb_{0.03}CO_3$	0.95	2.288	$4d^{10}$	1.69	$R\bar{3}c$	4.9129(6)		16.321(2)	341.15(9)
Rhodochrosite	$MnCO_3$	$Mn_{0.99}Fe_{0.01}CO_3$	0.83	2.195	$3d^5$	1.55	$R\bar{3}c$	4.7756(7)		15.669(2)	309.5(1)
Siderite	$FeCO_3$	$Fe_{0.98}Mg_{0.01}Mn_{0.01}CO_3$	0.78	2.142	$3d^6$	1.83	$R\bar{3}c$	4.6910(4)		15.3794(15)	293.10(6)
Smithsonite	$ZnCO_3$	$Zn_{0.97}Mg_{0.02}Ca_{0.01}CO_3$	0.74	2.11	$3d^{10}$	1.65	$R\bar{3}c$	4.65545(9)		15.0475(4)	282.44(1)
Spherocobaltite	$CoCO_3$	$Co_{0.55}Mg_{0.43}Ca_{0.01}CO_3$	0.745	2.109	$3d^7$	1.88	$R\bar{3}c$	4.6556(2)		15.013(1)	281.81(3)
Dolomite	$CaMg(CO_3)_2$	$Ca_{0.50}Mg_{0.50}CO_3$					$R\bar{3}$	4.8069(4)		16.0120(17)	320.42(6)

Table 1. Parameters of carbonate minerals. Chemical formulas are calculated from our EPMA measurements; ionic radiuses are from Shannon (1976); M–O bond distances for aragonite-group carbonates are from Ye et al. (2012); M–O bond distances for calcite-group carbonates are from Rutt and Nicola (1974); electronegativity values are from Haynes (2016); and unit cell parameters are from our XRD measurements. Measured data for aragonite, calcite, magnesite, rhodochrosite, siderite, and dolomite are from Farsang et al. (2018).

[a] Due to submicron size magnesite domains present in gaspeite, its formula shows a significant Mg content. However, Mg and Ni do not form solid solution in the mineral phase and gaspeite and magnesite peaks can be clearly distinguished in the Raman spectrum of the sample (Figure 3a). These two phases could also be distinguished by powder XRD and the unit cell parameters reported correspond to those of gaspeite only.

Always consult and cite the final, published document. See http:/www.minsocam.org or GeoscienceWorld

Mineral	Ideal formula	Raman-active mode frequency (cm^{-1})					
		External T	External L	Internal ν_4	Internal ν_1	Internal ν_3	Overtone
		E_g	E_g	E_g	A_{1g}	E_g	
Calcite	$CaCO_3$	158	284	713	1088	1438	1751
Gaspeite	$NiCO_3$	230	339	738	1090	1425	1735
Magnesite	$MgCO_3$	214	330	738	1094	1446	1763
Otavite	$CdCO_3$	161	272	714	1086	1390	1721
Rhodochrosite	$MnCO_3$	185	290	718	1086	1415	1727
Siderite	$FeCO_3$	183	284	731	1085		1724
Smithsonite	$ZnCO_3$	198	306	731	1093	1408	1736
Spherocobaltite	$CoCO_3$	206	313	730	1090	1443	1740

Table 2. Frequencies of Raman-active modes of calcite-group carbonate minerals at ambient pressure (1 bar) and temperature (25 ˚C). Data for calcite, magnesite, rhodochrosite, and siderite are from Farsang et al. (2018).

Always consult and cite the final, published document. See http:/www.minsocam.org or GeoscienceWorld

Mineral	Ideal formula	Pressure range of fit (GPa)	Pressure-induced shifts of Raman-active vibrational modes, $\delta\nu_i/\delta P$ (cm^{-1}/GPa)					
			External T	External L	Internal ν_4	Internal ν_1	Internal ν_3	Overtone
			E_g	E_g	E_g	A_{1g}	E_g	
Calcite	$CaCO_3$	0-5.9	2.42(4)	6.2(1)	2.2(1)	4.1(2)	5.68(9)	-0.7(5)
Gaspeite	$NiCO_3$	0-6.2	3.64(9)	4.9(2)	2.0(1)	2.8(1)	6.0(4)	-0.1(1)
Magnesite	$MgCO_3$	0-5.9	3.52(3)	4.89(3)	1.52(4)	2.87(4)	4.3(1)	0.21(3)
Otavite	$CdCO_3$	0-6.2	3.58(8)	5.11(6)	2.13(6)	3.97(5)	5.38(7)	-0.64(7)
Rhodochrosite	$MnCO_3$	0-6.3	3.38(6)	4.83(8)	2.03(4)	3.34(5)	4.64(7)	-0.92(7)
Siderite	$FeCO_3$	0-6.2	3.98(9)	4.52(5)	2.4(2)	2.60(7)		-0.8(1)
Smithsonite	$ZnCO_3$	0-6.3	3.5(1)	4.4(1)	2.06(9)	3.13(9)	4.5(1)	0.10(7)
Spherocobaltite	$CoCO_3$	0-6.2	4.0(1)	4.6(1)	1.8(1)	2.64(9)	5.0(3)	0.0(1)

Table 3. Pressure-induced shifts of Raman-active vibrational modes of calcite-group carbonate minerals. Data for calcite, magnesite, rhodochrosite, and siderite are from Farsang et al. (2018).

Always consult and cite the final, published document. See http:/www.minsocam.org or GeoscienceWorld

Mineral	Ideal formula	Temperature range of fit (˚C)	Temperature-induced shifts of Raman-active vibrational modes, $\delta\nu_i/\delta T$ (cm^{-1}/K)					
			External T	External L	Internal ν_4	Internal ν_1	Internal ν_3	Overtone
			E_g	E_g	E_g	A_{1g}	E_g	
Calcite	$CaCO_3$	25-500	$-2.65(2)\times10^{-2}$	$-4.30(4)\times10^{-2}$	$-5.0(2)\times10^{-3}$	$-9.7(3)\times10^{-3}$	$-2.40(7)\times10^{-2}$	$-1.36(6)\times10^{-2}$
Gaspeite	$NiCO_3$	25-350	$-1.3(1)\times10^{-2}$	$-2.6(1)\times10^{-2}$	$1.5(2)\times10^{-3}$	$-1(1)\times10^{-3}$	$-1.7(2)\times10^{-2}$	$-1.7(2)\times10^{-2}$
Magnesite	$MgCO_3$	25-500	$-2.05(5)\times10^{-2}$	$-3.01(5)\times10^{-2}$	$-2.0(8)\times10^{-3}$	$-1.4(7)\times10^{-3}$	$-1.7(1)\times10^{-2}$	$-1.63(8)\times10^{-2}$
Otavite	$CdCO_3$	25-375	$-2.1(2)\times10^{-2}$	$-2.7(1)\times10^{-2}$	$0(1)\times10^{-3}$	$-1.0(1)\times10^{-2}$	$-1.7(1)\times10^{-2}$	$-1.8(1)\times10^{-2}$
Rhodochrosite	$MnCO_3$	25-400	$-1.98(6)\times10^{-2}$	$-2.93(6)\times10^{-2}$	$1.4(8)\times10^{-3}$	$-5.8(7)\times10^{-3}$	$-1.40(5)\times10^{-2}$	$-1.3(1)\times10^{-2}$
Siderite	$FeCO_3$	25-375	$1(1)\times10^{-3}$	$-1.0(1)\times10^{-2}$	$-1.35(9)\times10^{-2}$	$-3(1)\times10^{-3}$		$-1.6(1)\times10^{-2}$
Smithsonite	$ZnCO_3$	25-350	$-3.21(7)\times10^{-2}$	$-2.72(3)\times10^{-2}$	$-3.4(4)\times10^{-3}$	$-9.5(6)\times10^{-3}$	$-1.69(8)\times10^{-2}$	$-2.06(8)\times10^{-2}$
Spherocobaltite	$CoCO_3$	25-425	$-1.76(6)\times10^{-2}$	$-1.91(9)\times10^{-2}$	$-1.9(7)\times10^{-3}$	$-8.0(5)\times10^{-3}$	$-3.8(9)\times10^{-2}$	$-1.5(2)\times10^{-2}$

Table 4. Temperature-induced shifts of Raman-active vibrational modes of calcite-group carbonate minerals. Data for calcite, magnesite, rhodochrosite, and siderite are from Farsang et al. (2018).

Always consult and cite the final, published document. See http:/www.minsocam.org or GeoscienceWorld

Mineral	K_T (GPa)	K_S (GPa)	α ($\times10^{-5}$ K^{-1})	C_P ($Jmol^{-1}K^{-1}$)	ρ ($molm^{-3}$)	γ
Aragonite	65.7±0.8[a]	68.9±1.4[k]	6.5±1[q]	83.1[t]	29254	1.84
Cerussite	63±2[b]	72.4[l]	8.0±3[q]	87.07±0.09[u]	24543	2.71
Strontianite	62±1[c]	64±4[l]	6.8±1[q]	86.52±0.15[v]	25894	1.94
Witherite	48±1[c]	58.7[l]	6.5±2[q]	93.24±0.17[w]	21871	1.87
Calcite	73.46±0.27[d]	76.1[m]	1.30±0.12[r]	83.4708[x]	27138	0.44
Gaspeite	131±1[e]					
Magnesite	107±1[e]	115.7±1.0[n]	3.81±0.38[r]	76.09[y]	35581	1.63
Otavite	101±3[f]		1.80±4[r]			
Rhodochrosite	110±11[g]	108.5±1.8[o]	2.09±0.19[r]	80.62±0.10[z]	32193	0.87
Siderite	117±1[e]	115.5±1.5[n]	2.98[s]	83.26±2[aa]	33993	1.23
Smithsonite	126.8±0.6[h]		3.66±0.13[r]	80.05[ab]	35276	
Spherocobaltite	128±2[i]					
Dolomite	94.1±0.7[j]	94.8[p]	2.41[s]	157.5±0.4[ac]	15547	0.93

Table 5. Thermodynamic properties and macroscopic Grüneisen parameters of carbonate minerals. Isothermal bulk moduli (K_T) are from: a (Litasov et al. 2017), b (Gao et al. 2016), c (Wang et al. 2015), d (Redfern and Angel 1999), e (Zhang and Reeder 1999), f (Minch et al. 2010a), g (Boulard et al. 2015), h (Gao et al. 2014), i (Chariton et al. 2018), j (Ross and Reeder 1992). Adiabatic bulk moduli (K_S) are from: k (Liu et al. 2005), l (Biedermann et al. 2017b), m (Chen et al. 2001), n (Sanchez-Valle et al. 2011), o (Zhao et al. 2018), p (Humbert and Plicque 1972). Thermal expansion coefficients (α) are from: q (Ye et al. 2012), r (Wang et al. 2019a), s (Zhang et al. 1998), s (Reeder and Markgraf 1986). Heat capacities at constant pressure (C_P) are from: t (Ungureanu et al. 2010), u (Bissengaliyeva et al. 2012), v (Gurevich et al. 2001a), w (Gurevich et al. 2001b), x (Staveley and Linford 1969), y (Hemingway et al. 1977), z (Robie et al. 1984), aa (Bénézeth et al. 2009), ab (Haselton and Goldsmith 1987), ac (Stout and Robie 1963). Molar densities (ρ) are calculated from measured unit cell parameters (Table 1).

Always consult and cite the final, published document. See http:/www.minsocam.org or GeoscienceWorld

Fig. 1

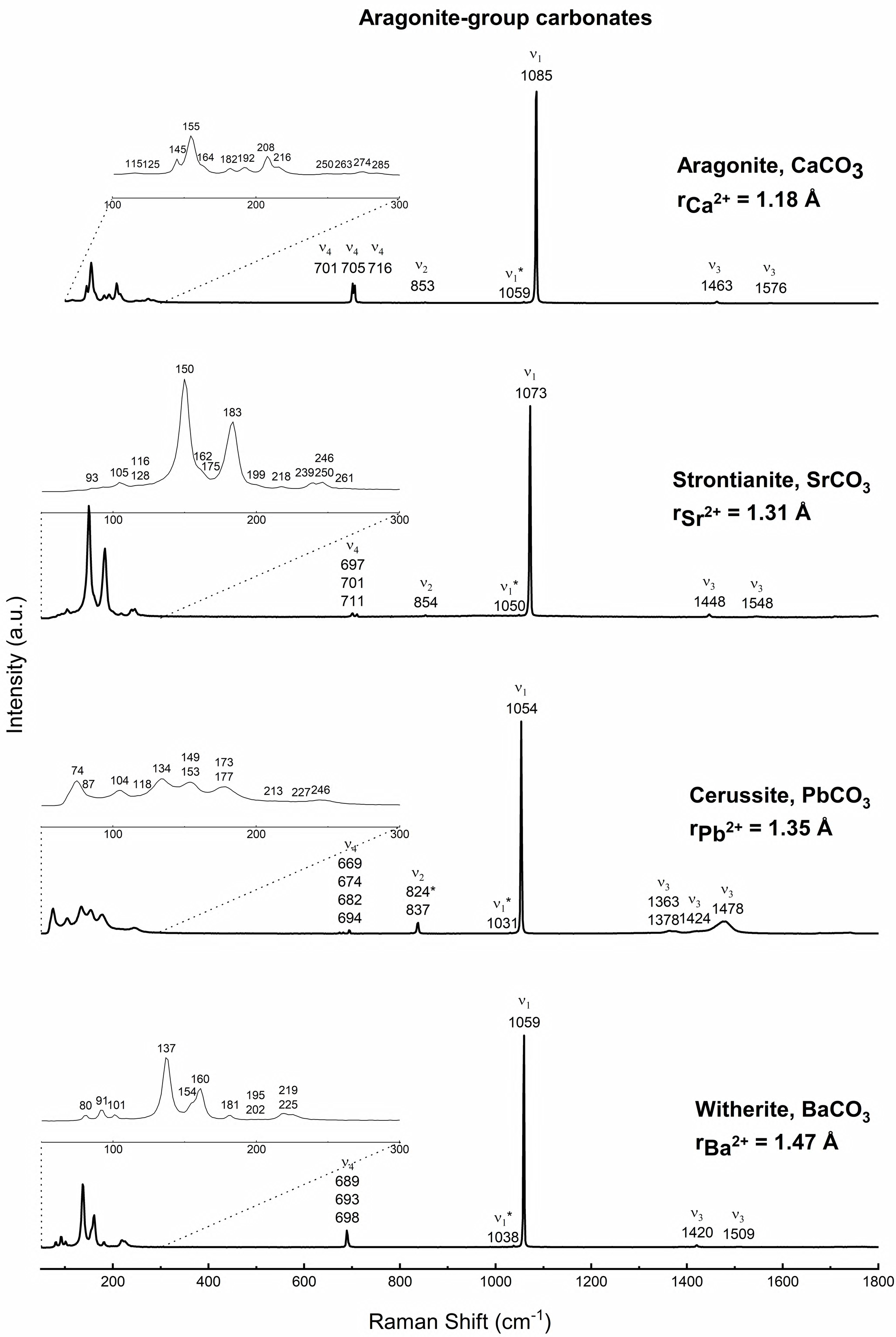
Aragonite-group carbonates
Aragonite, CaCO3
rCa2+ = 1.18 Å
Strontianite, SrCO3
rSr2+ = 1.31 Å
Cerussite, PbCO3
rPb2+ = 1.35 Å
Witherite, BaCO3
rBa2+ = 1.47 Å
Intensity (a.u.)
Raman Shift (cm-1)

Fig. 2

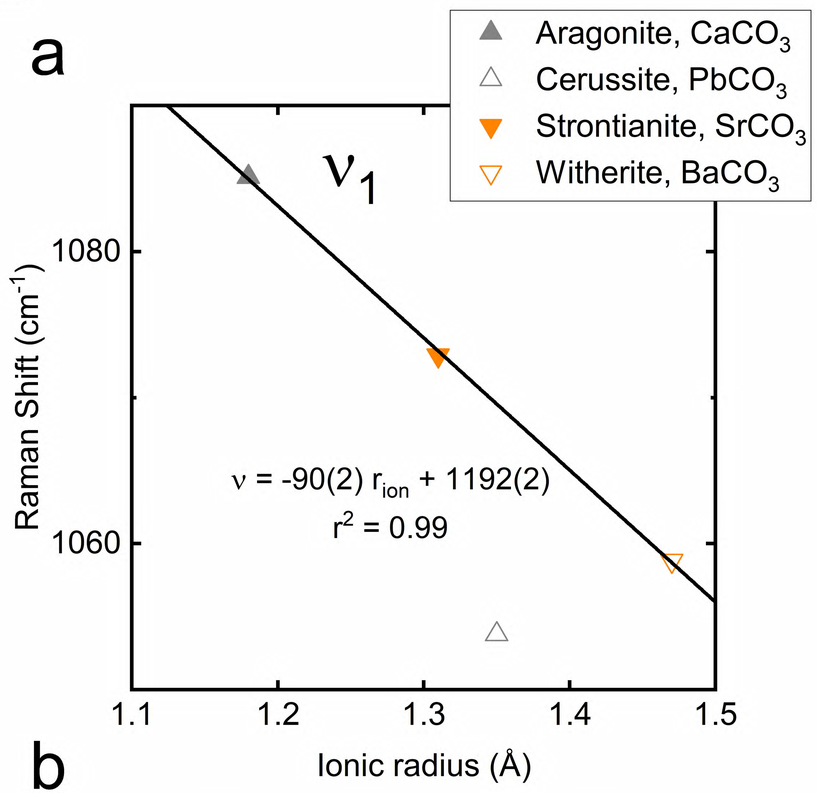
a
Aragonite, $CaCO_3$
Cerussite, $PbCO_3$
Strontianite, $SrCO_3$
Witherite, $BaCO_3$
ν_1
ν = -90(2) r_{ion} + 1192(2)
r^2 = 0.99
Raman Shift (cm^{-1})
1080
1060
1.1
1.2
1.3
1.4
1.5
Ionic radius (Å)

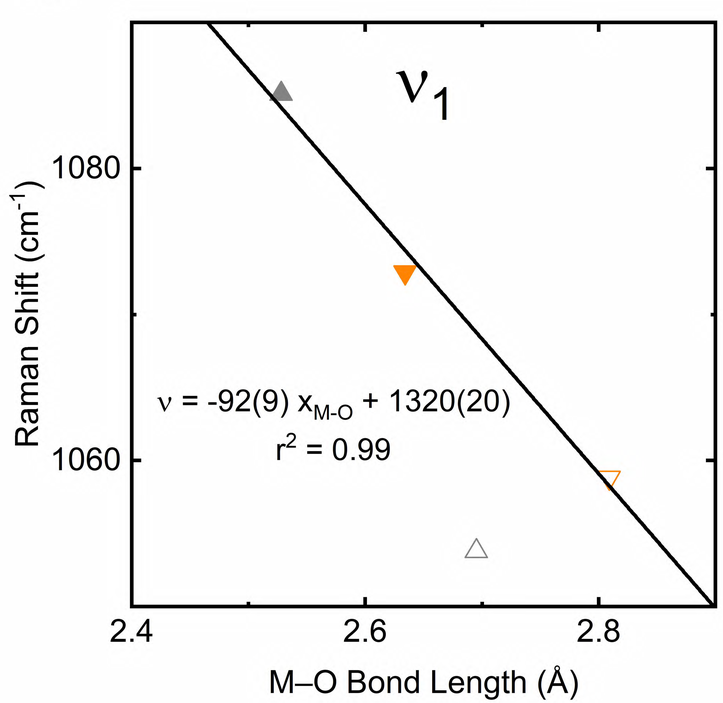
b
ν_1
ν = -92(9) x_{M-O} + 1320(20)
r^2 = 0.99
Raman Shift (cm^{-1})
1080
1060
2.4
2.6
2.8
M–O Bond Length (Å)

Fig. 3a

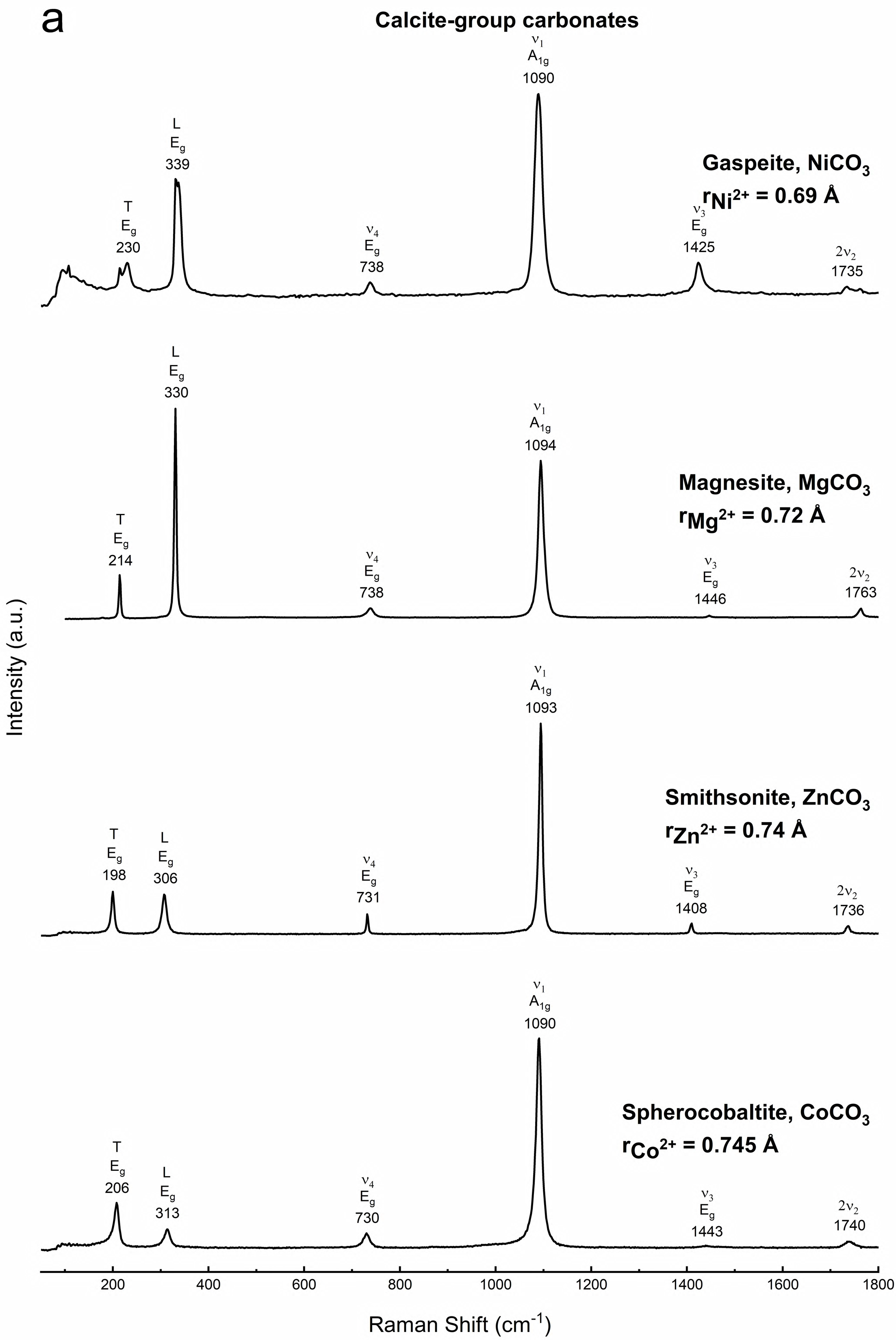
a
Calcite-group carbonates
Gaspeite, NiCO3
rNi2+ = 0.69 Å
T Eg 230
L Eg 339
ν4 Eg 738
ν1 A1g 1090
ν3 Eg 1425
2ν2 1735
Magnesite, MgCO3
rMg2+ = 0.72 Å
T Eg 214
L Eg 330
ν4 Eg 738
ν1 A1g 1094
ν3 Eg 1446
2ν2 1763
Smithsonite, ZnCO3
rZn2+ = 0.74 Å
T Eg 198
L Eg 306
ν4 Eg 731
ν1 A1g 1093
ν3 Eg 1408
2ν2 1736
Spherocobaltite, CoCO3
rCo2+ = 0.745 Å
T Eg 206
L Eg 313
ν4 Eg 730
ν1 A1g 1090
ν3 Eg 1443
2ν2 1740
Intensity (a.u.)
200
400
600
800
1000
1200
1400
1600
1800
Raman Shift (cm-1)

Fig. 3b

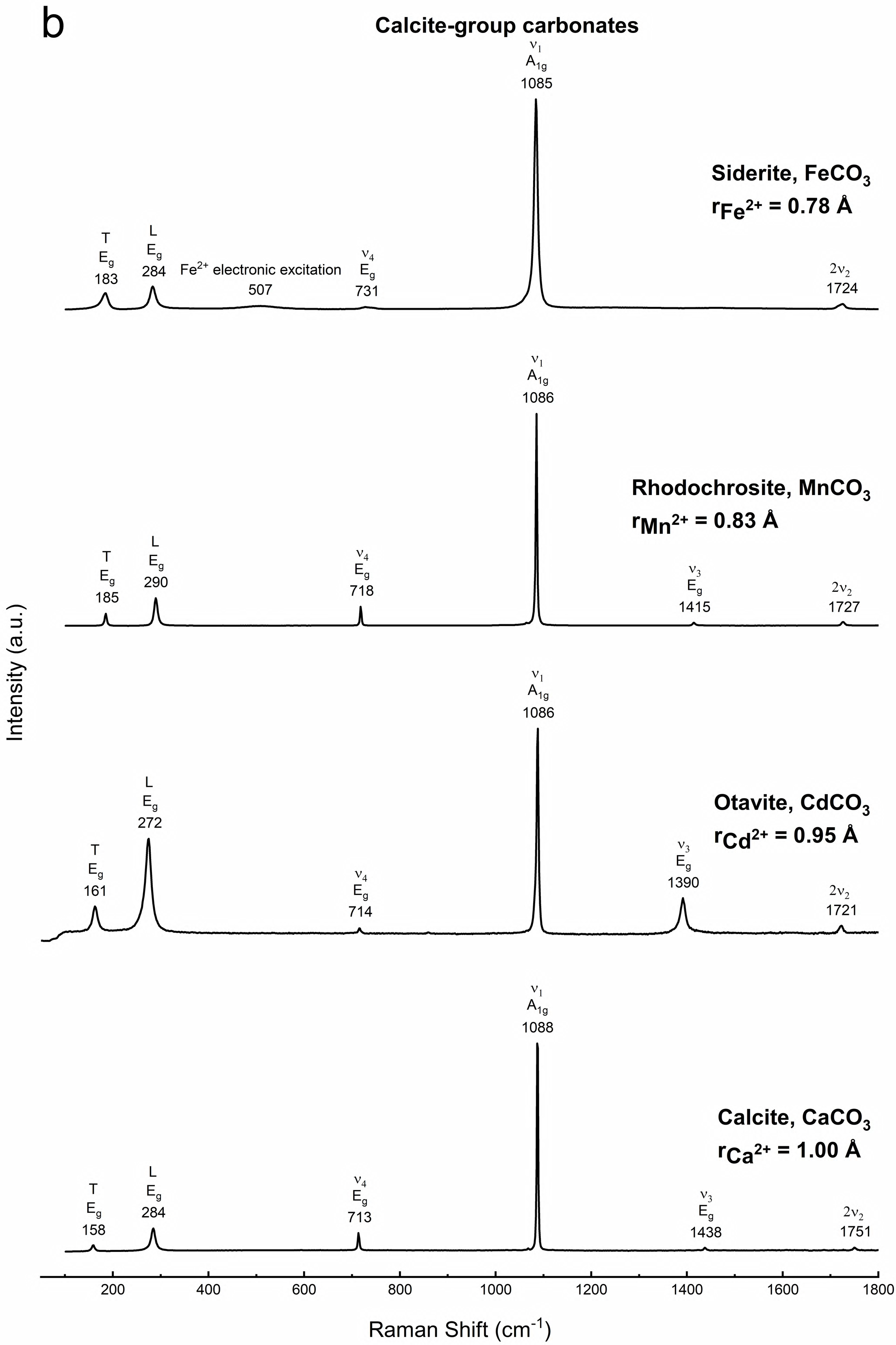
b
Calcite-group carbonates
Siderite, FeCO3
rFe2+ = 0.78 Å
T Eg 183
L Eg 284
Fe2+ electronic excitation 507
ν4 Eg 731
ν1 A1g 1085
2ν2 1724
Rhodochrosite, MnCO3
rMn2+ = 0.83 Å
T Eg 185
L Eg 290
ν4 Eg 718
ν1 A1g 1086
ν3 Eg 1415
2ν2 1727
Otavite, CdCO3
rCd2+ = 0.95 Å
T Eg 161
L Eg 272
ν4 Eg 714
ν1 A1g 1086
ν3 Eg 1390
2ν2 1721
Calcite, CaCO3
rCa2+ = 1.00 Å
T Eg 158
L Eg 284
ν4 Eg 713
ν1 A1g 1088
ν3 Eg 1438
2ν2 1751
Intensity (a.u.)
200
400
600
800
1000
1200
1400
1600
1800
Raman Shift (cm-1)

Fig. 4

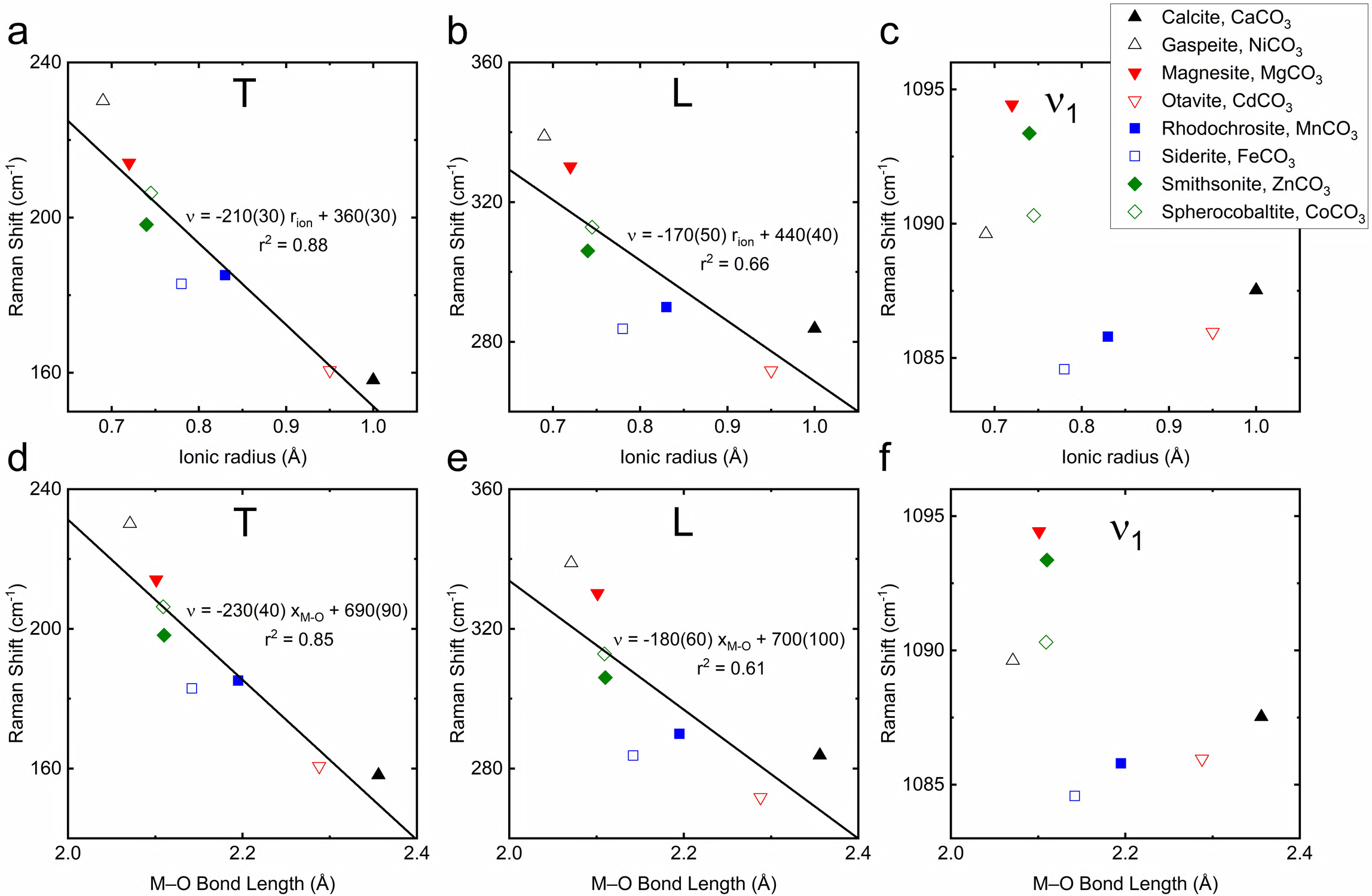
a
T
ν = -210(30) r_ion + 360(30)
r² = 0.88
Raman Shift (cm⁻¹)
Ionic radius (Å)
b
L
ν = -170(50) r_ion + 440(40)
r² = 0.66
c
ν1
Calcite, CaCO3
Gaspeite, NiCO3
Magnesite, MgCO3
Otavite, CdCO3
Rhodochrosite, MnCO3
Siderite, FeCO3
Smithsonite, ZnCO3
Spherocobaltite, CoCO3
d
T
ν = -230(40) x_M-O + 690(90)
r² = 0.85
M–O Bond Length (Å)
e
L
ν = -180(60) x_M-O + 700(100)
r² = 0.61
f
ν1

Fig. 5

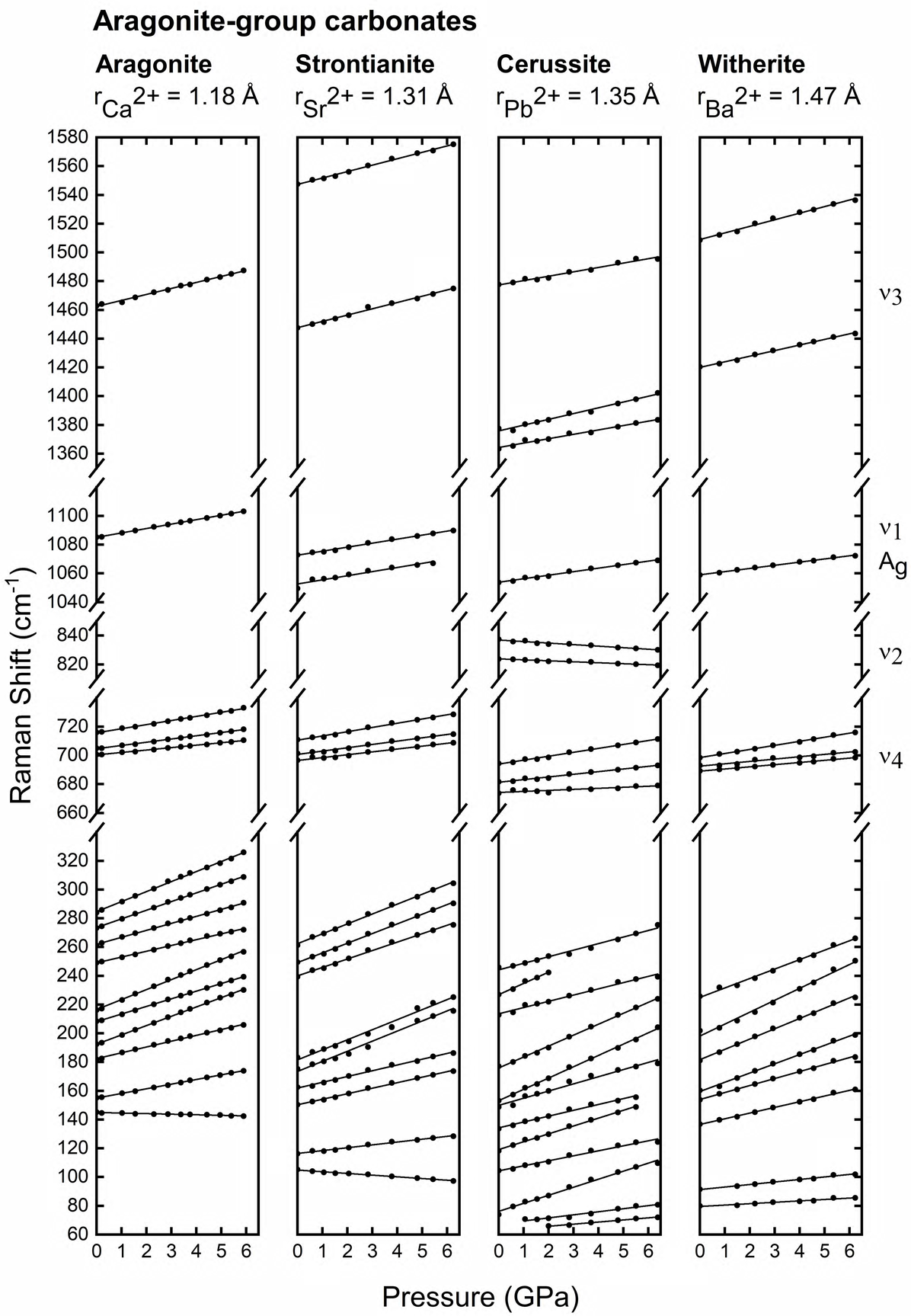
Aragonite-group carbonates
Aragonite
$r_{Ca}2+$ = 1.18 Å
Strontianite
$r_{Sr}2+$ = 1.31 Å
Cerussite
$r_{Pb}2+$ = 1.35 Å
Witherite
$r_{Ba}2+$ = 1.47 Å
Raman Shift (cm^{-1})
Pressure (GPa)
ν3
ν1
Ag
ν2
ν4

Fig 6

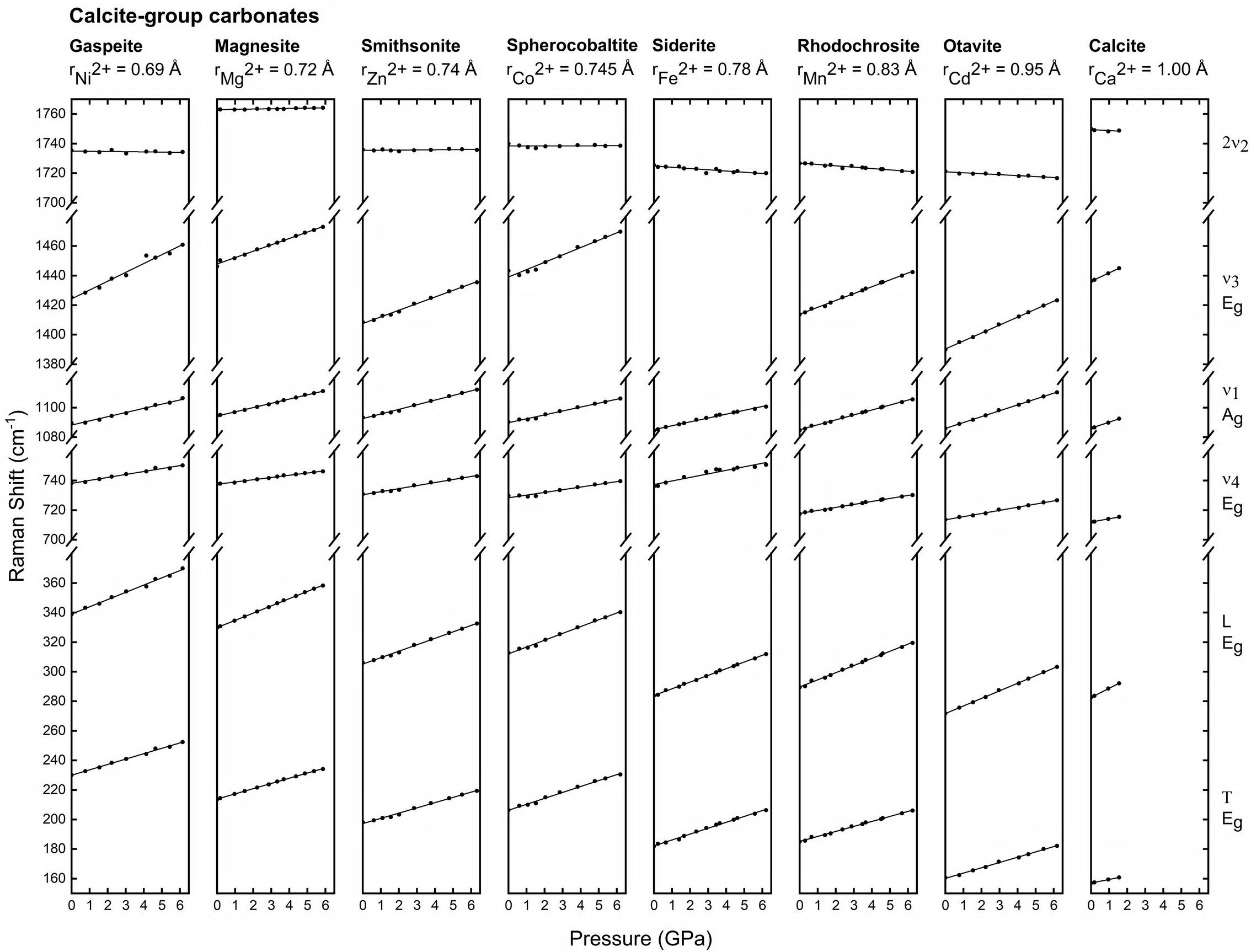
Calcite-group carbonates
Gaspeite
$r_{Ni}2+$ = 0.69 Å
Magnesite
$r_{Mg}2+$ = 0.72 Å
Smithsonite
$r_{Zn}2+$ = 0.74 Å
Spherocobaltite
$r_{Co}2+$ = 0.745 Å
Siderite
$r_{Fe}2+$ = 0.78 Å
Rhodochrosite
$r_{Mn}2+$ = 0.83 Å
Otavite
$r_{Cd}2+$ = 0.95 Å
Calcite
$r_{Ca}2+$ = 1.00 Å
Raman Shift (cm^{-1})
Pressure (GPa)
$2\nu_2$
ν_3 E_g
ν_1 A_g
ν_4 E_g
L E_g
T E_g

Fig. 7

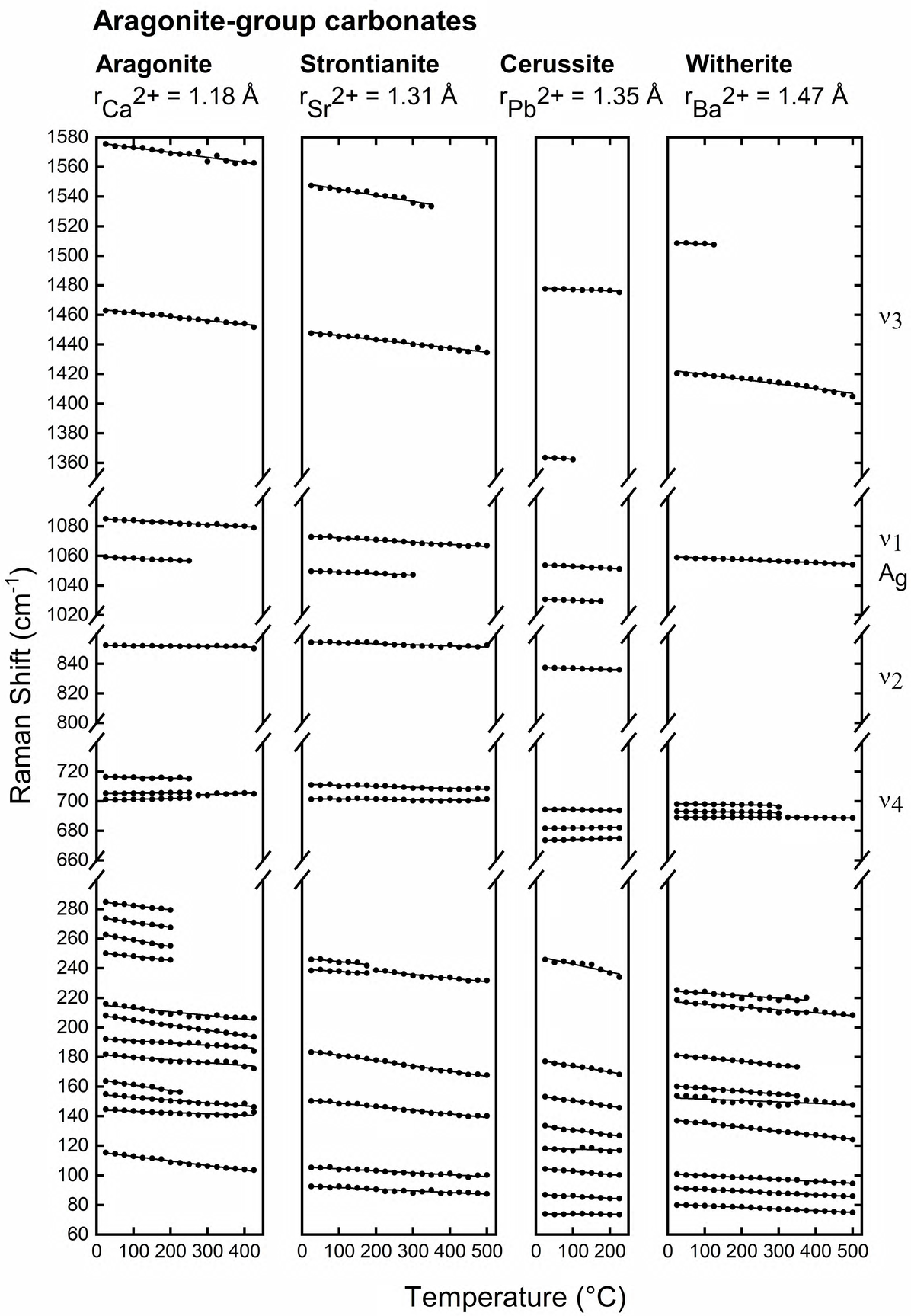
Aragonite-group carbonates
Aragonite
$r_{Ca}2+$ = 1.18 Å
Strontianite
$r_{Sr}2+$ = 1.31 Å
Cerussite
$r_{Pb}2+$ = 1.35 Å
Witherite
$r_{Ba}2+$ = 1.47 Å
Raman Shift (cm^{-1})
Temperature (°C)
ν3
ν1
Ag
ν2
ν4

Fig 8

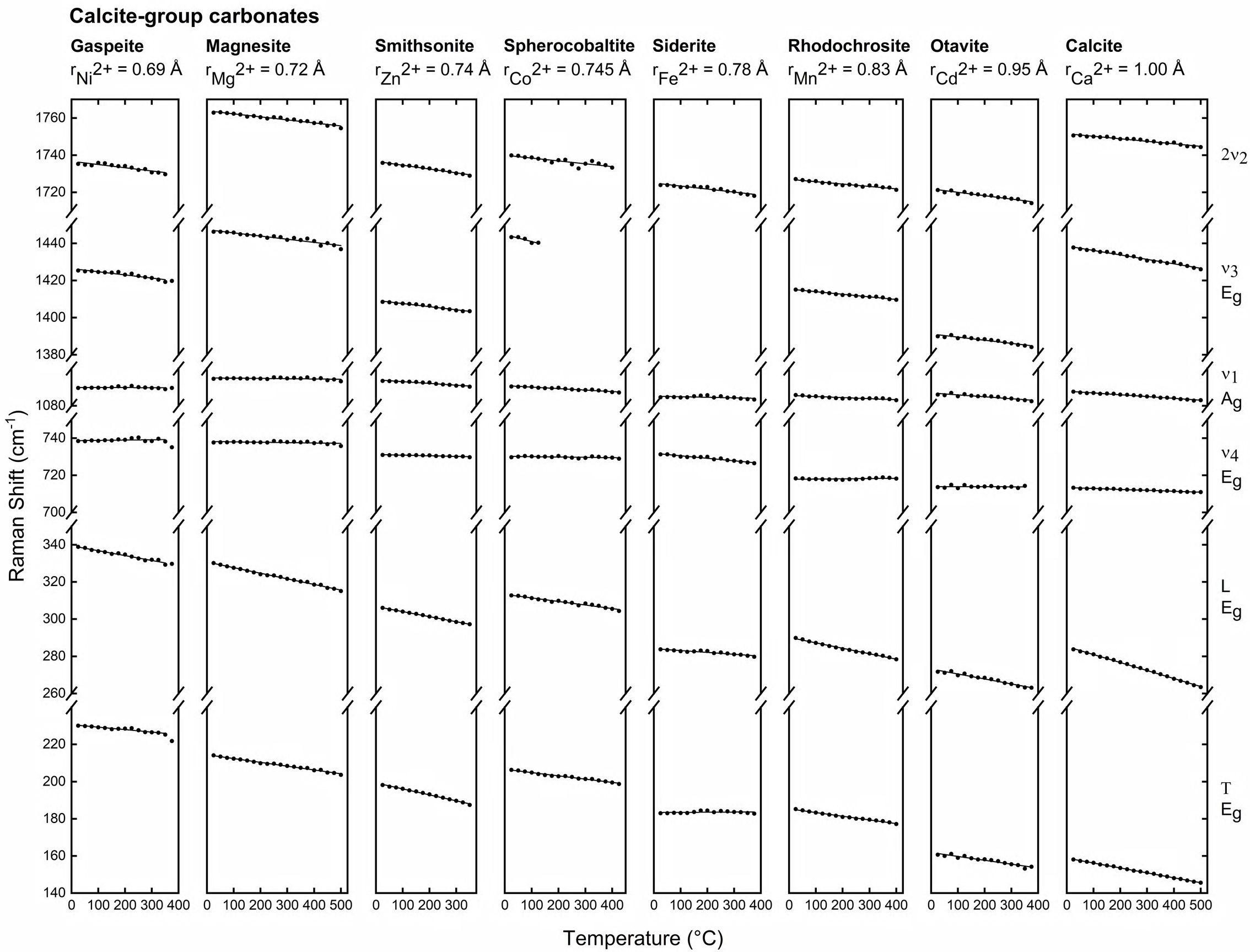
Calcite-group carbonates
Gaspeite
$r_{Ni}2+$ = 0.69 Å
Magnesite
$r_{Mg}2+$ = 0.72 Å
Smithsonite
$r_{Zn}2+$ = 0.74 Å
Spherocobaltite
$r_{Co}2+$ = 0.745 Å
Siderite
$r_{Fe}2+$ = 0.78 Å
Rhodochrosite
$r_{Mn}2+$ = 0.83 Å
Otavite
$r_{Cd}2+$ = 0.95 Å
Calcite
$r_{Ca}2+$ = 1.00 Å
Raman Shift (cm^{-1})
Temperature (°C)
$2\nu_2$
ν_3 E_g
ν_1 A_g
ν_4 E_g
L E_g
T E_g

Fig. 9

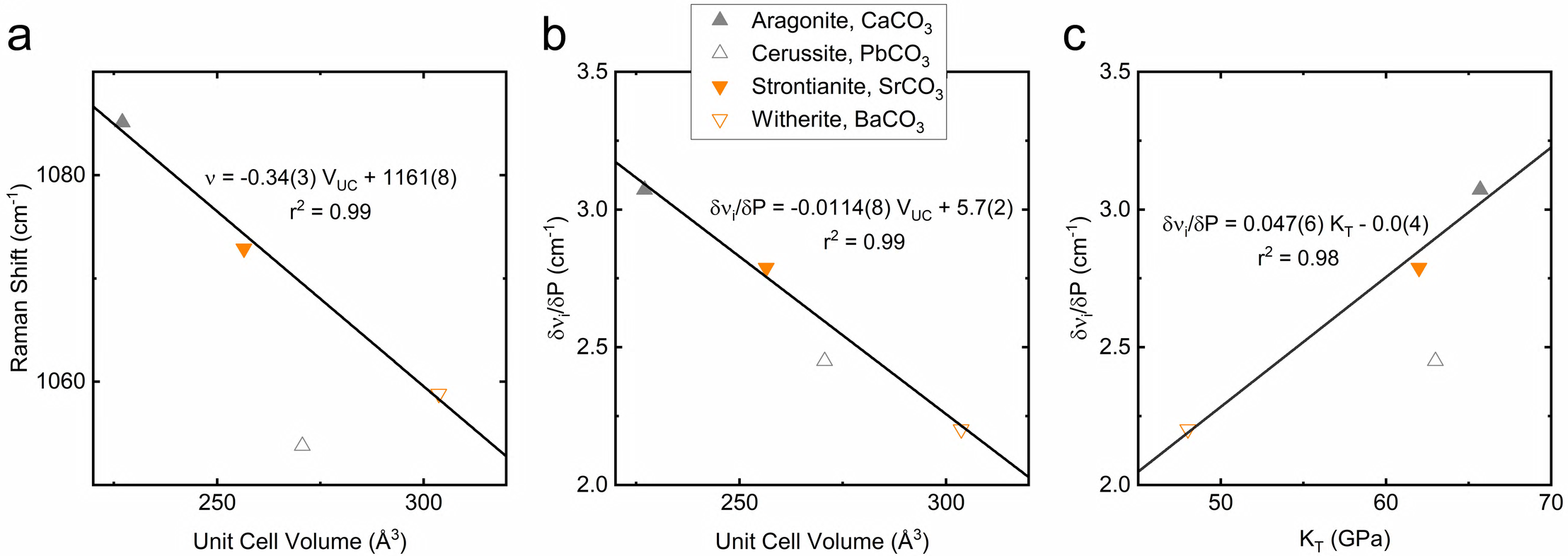
a
b
c
Aragonite, CaCO3
Cerussite, PbCO3
Strontianite, SrCO3
Witherite, BaCO3
ν = -0.34(3) VUC + 1161(8)
r2 = 0.99
δνi/δP = -0.0114(8) VUC + 5.7(2)
r2 = 0.99
δνi/δP = 0.047(6) KT - 0.0(4)
r2 = 0.98
Raman Shift (cm-1)
δνi/δP (cm-1)
Unit Cell Volume (Å3)
KT (GPa)
1080
1060
250
300
3.5
3.0
2.5
2.0
50
60
70

Fig. 10a-c

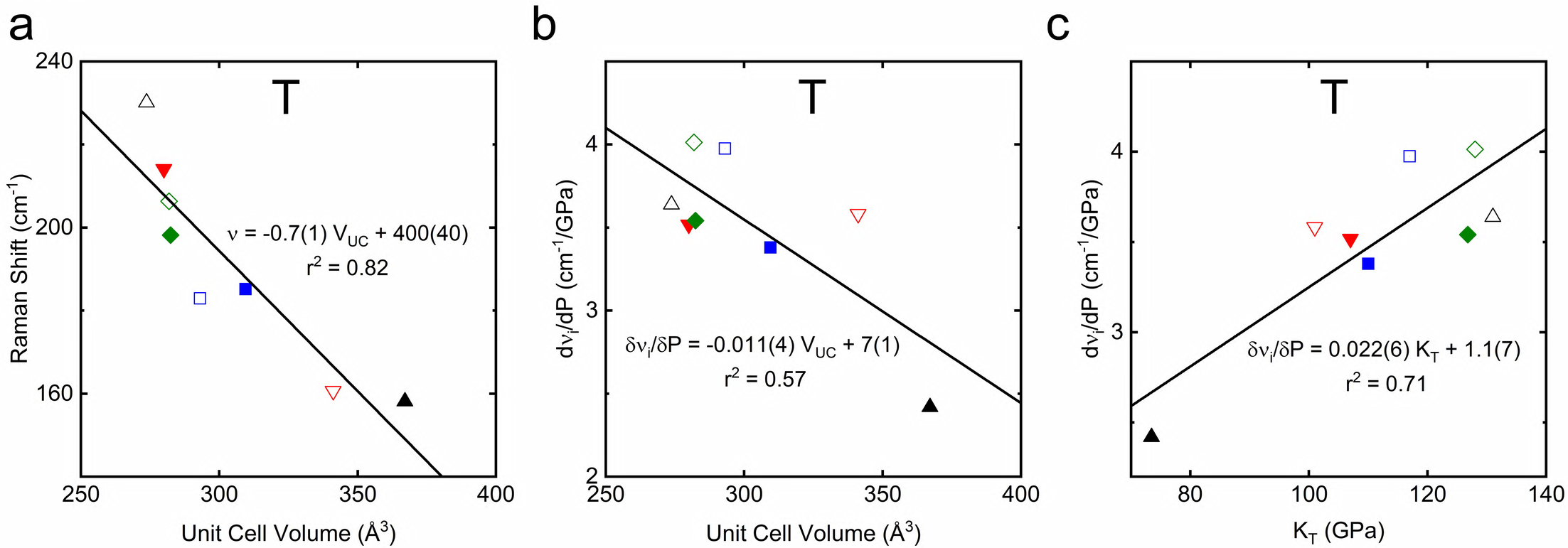
a
b
c
T
T
T
ν = -0.7(1) V_UC + 400(40)
r² = 0.82
δν_i/δP = -0.011(4) V_UC + 7(1)
r² = 0.57
δν_i/δP = 0.022(6) K_T + 1.1(7)
r² = 0.71
Raman Shift (cm⁻¹)
dν_i/dP (cm⁻¹/GPa)
dν_i/dP (cm⁻¹/GPa)
Unit Cell Volume (Å³)
Unit Cell Volume (Å³)
K_T (GPa)
240
200
160
4
3
2
4
3
250
300
350
400
250
300
350
400
80
100
120
140

Fig. 10d-f

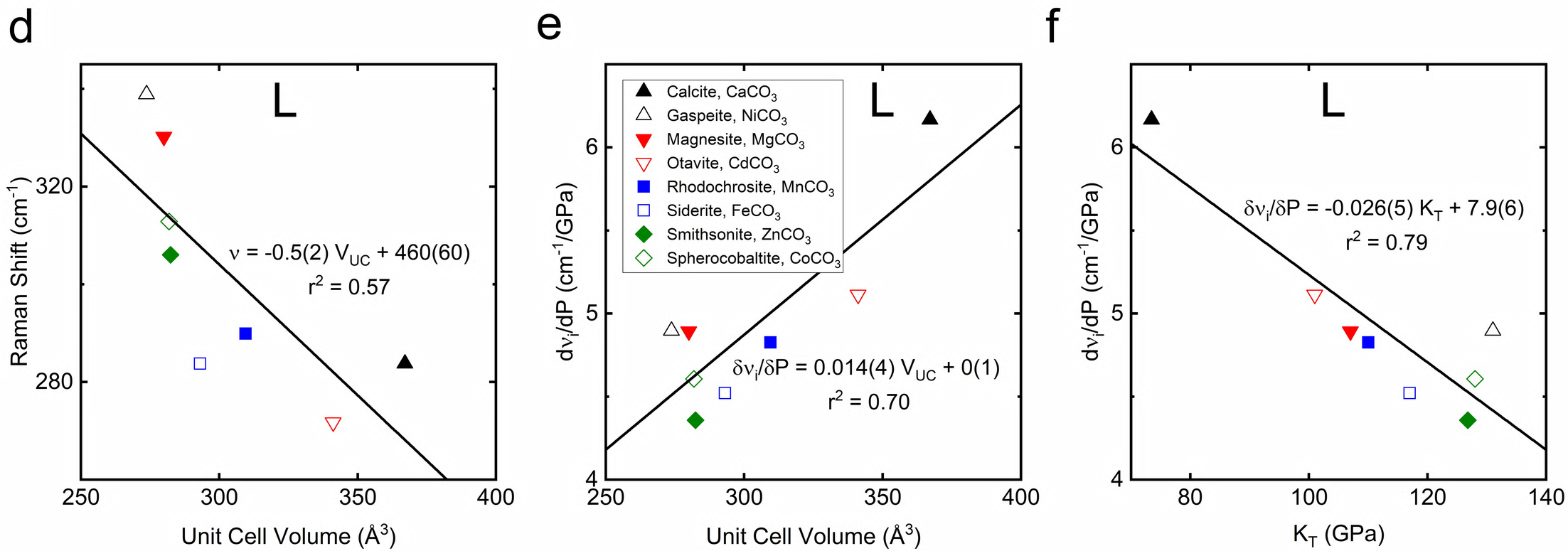
d
e
f
L
L
L
Raman Shift (cm-1)
Unit Cell Volume (Å3)
ν = -0.5(2) VUC + 460(60)
r2 = 0.57
dνi/dP (cm-1/GPa)
Unit Cell Volume (Å3)
δνi/δP = 0.014(4) VUC + 0(1)
r2 = 0.70
Calcite, CaCO3
Gaspeite, NiCO3
Magnesite, MgCO3
Otavite, CdCO3
Rhodochrosite, MnCO3
Siderite, FeCO3
Smithsonite, ZnCO3
Spherocobaltite, CoCO3
dνi/dP (cm-1/GPa)
KT (GPa)
δνi/δP = -0.026(5) KT + 7.9(6)
r2 = 0.79

Fig. 10g-i

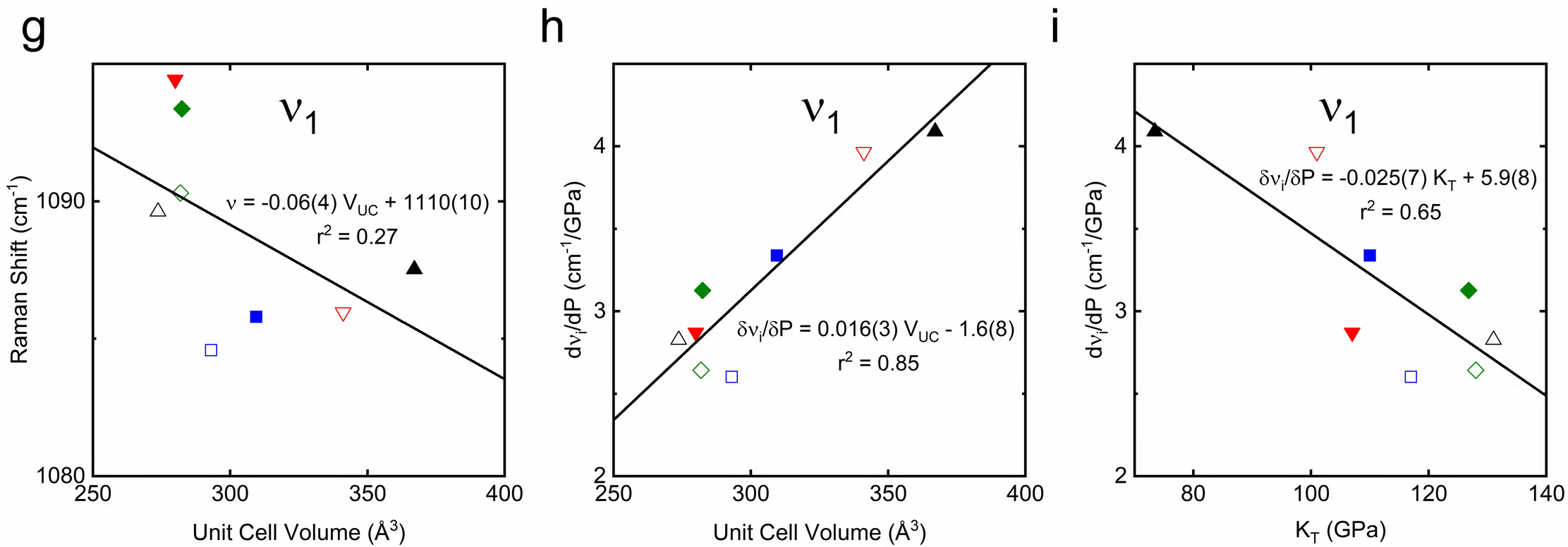
g
h
i
ν1
ν = -0.06(4) VUC + 1110(10)
r2 = 0.27
Raman Shift (cm-1)
1090
1080
250
300
350
400
Unit Cell Volume (Å3)
ν1
δνi/δP = 0.016(3) VUC - 1.6(8)
r2 = 0.85
dνi/dP (cm-1/GPa)
4
3
2
250
300
350
400
Unit Cell Volume (Å3)
ν1
δνi/δP = -0.025(7) KT + 5.9(8)
r2 = 0.65
dνi/dP (cm-1/GPa)
4
3
2
80
100
120
140
KT (GPa)

Fig. 11

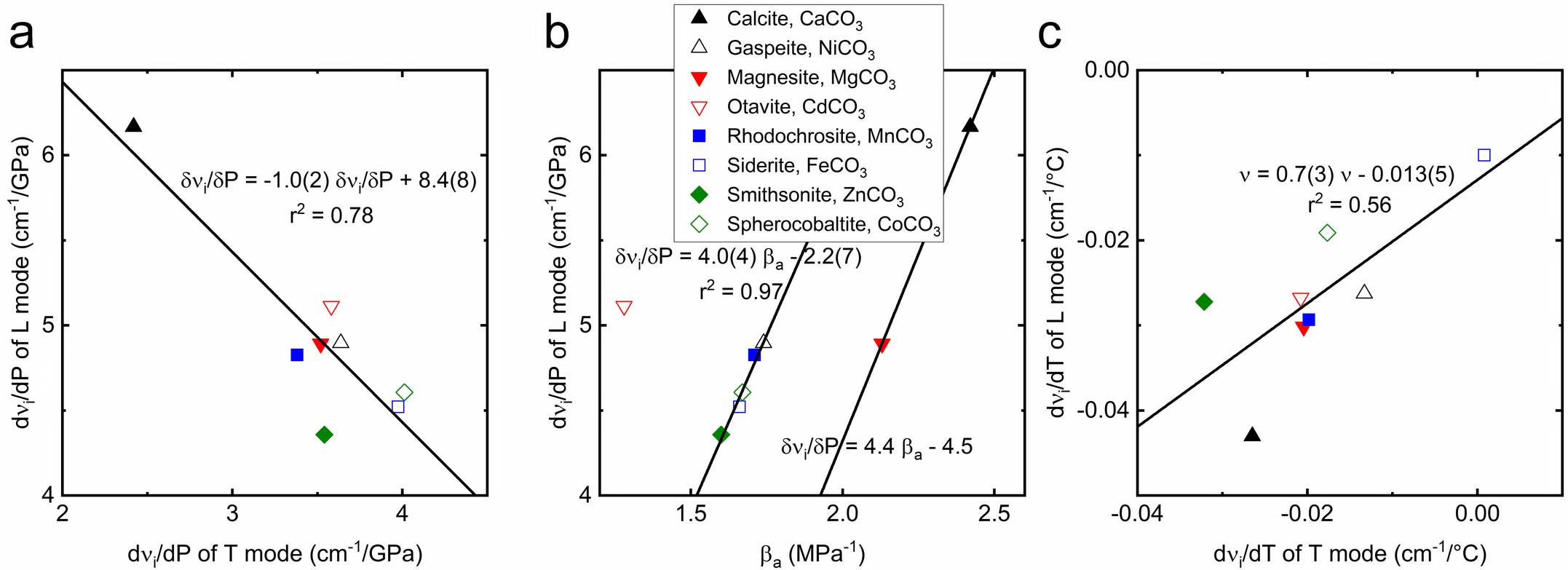
a
b
c
Calcite, CaCO3
Gaspeite, NiCO3
Magnesite, MgCO3
Otavite, CdCO3
Rhodochrosite, MnCO3
Siderite, FeCO3
Smithsonite, ZnCO3
Spherocobaltite, CoCO3
δνi/δP = -1.0(2) δνi/δP + 8.4(8)
r2 = 0.78
δνi/δP = 4.0(4) βa - 2.2(7)
r2 = 0.97
δνi/δP = 4.4 βa - 4.5
ν = 0.7(3) ν - 0.013(5)
r2 = 0.56
dνi/dP of L mode (cm-1/GPa)
dνi/dP of T mode (cm-1/GPa)
βa (MPa-1)
dνi/dT of L mode (cm-1/°C)
dνi/dT of T mode (cm-1/°C)

Fig. 12

a

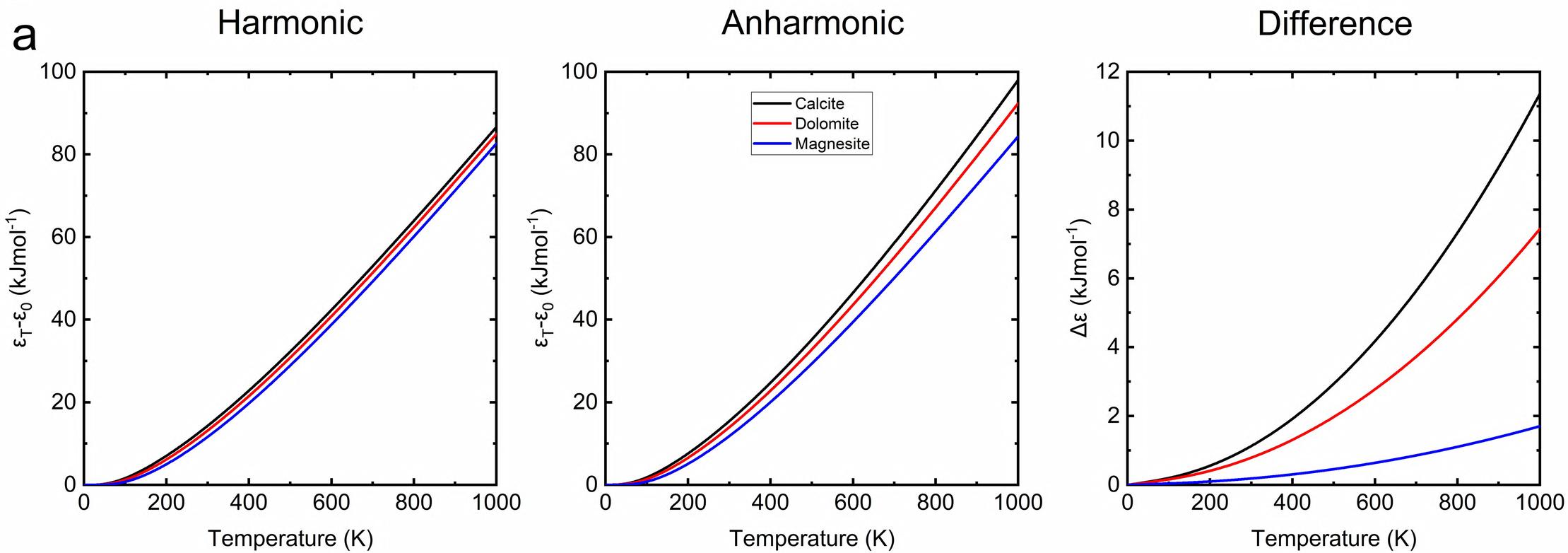
Harmonic
Anharmonic
Difference
Calcite
Dolomite
Magnesite
ε_T-ε_0 (kJmol^{-1})
$\Delta\varepsilon$ (kJmol^{-1})
Temperature (K)
0
200
400
600
800
1000
20
40
60
80
100
2
4
6
8
10
12

Fig. 12

b

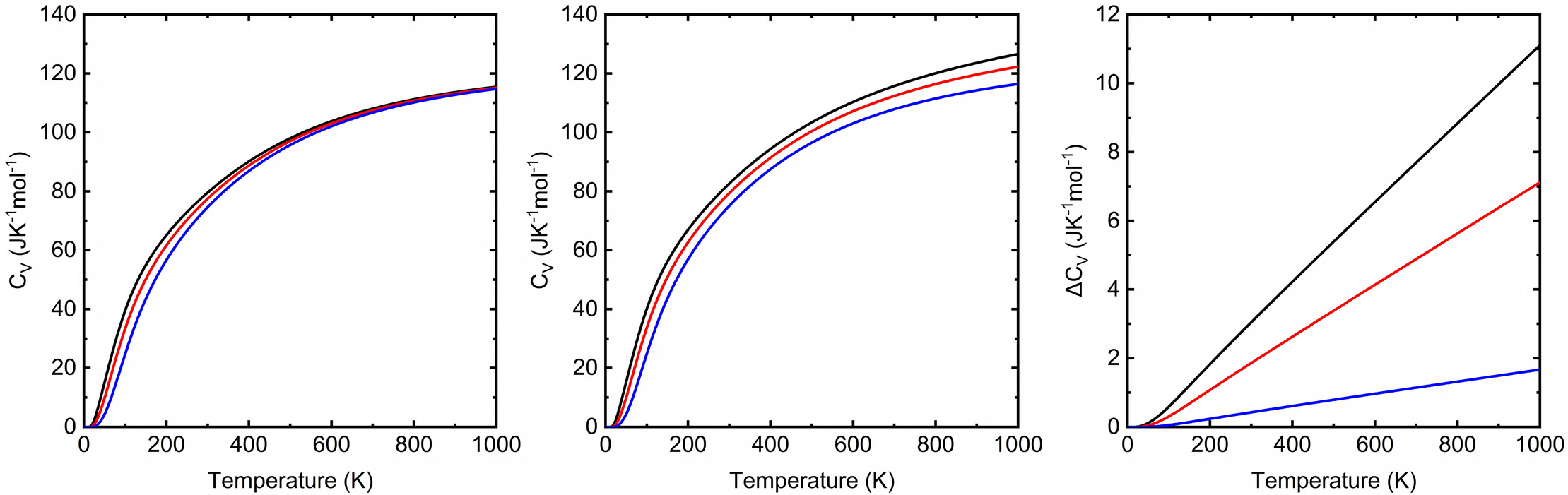
140
120
100
80
60
40
20
0
C_V ($JK^{-1}mol^{-1}$)
0
200
400
600
800
1000
Temperature (K)
140
120
100
80
60
40
20
0
C_V ($JK^{-1}mol^{-1}$)
0
200
400
600
800
1000
Temperature (K)
12
10
8
6
4
2
0
ΔC_V ($JK^{-1}mol^{-1}$)
0
200
400
600
800
1000
Temperature (K)

Fig. 12

c

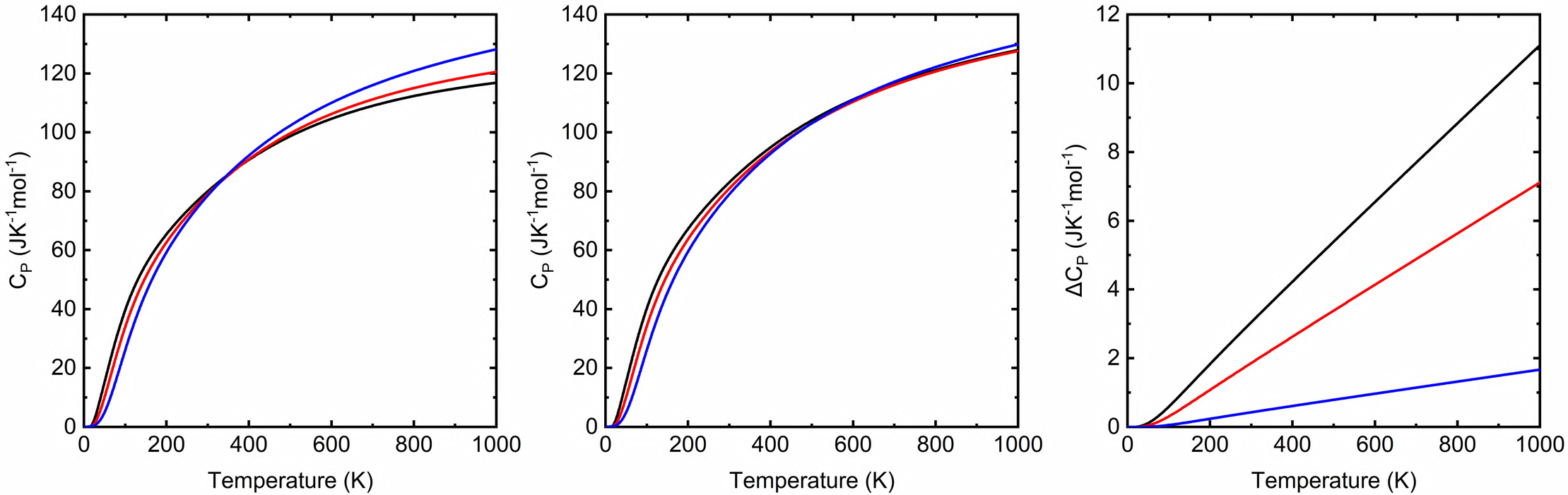
140
120
100
80
60
40
20
0
C_P ($JK^{-1}mol^{-1}$)
0
200
400
600
800
1000
Temperature (K)
140
120
100
80
60
40
20
0
C_P ($JK^{-1}mol^{-1}$)
0
200
400
600
800
1000
Temperature (K)
12
10
8
6
4
2
0
ΔC_P ($JK^{-1}mol^{-1}$)
0
200
400
600
800
1000
Temperature (K)

Fig. 12

d

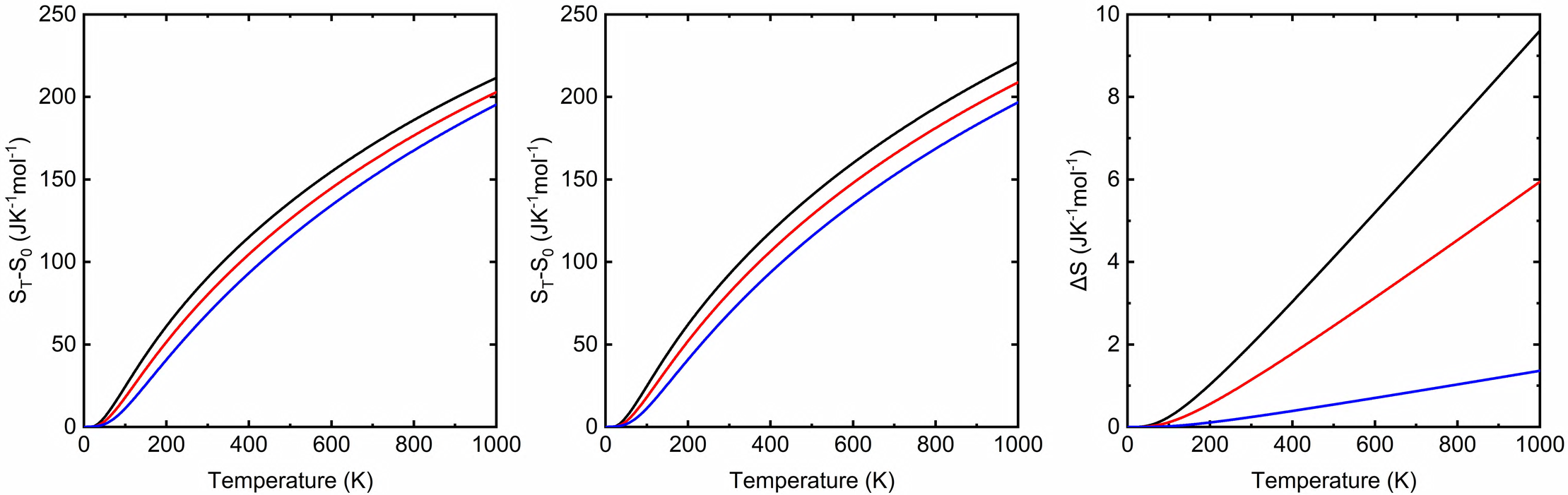
250
200
150
100
50
0
S_T-S_0 ($JK^{-1}mol^{-1}$)
0
200
400
600
800
1000
Temperature (K)
250
200
150
100
50
0
S_T-S_0 ($JK^{-1}mol^{-1}$)
0
200
400
600
800
1000
Temperature (K)
10
8
6
4
2
0
ΔS ($JK^{-1}mol^{-1}$)
0
200
400
600
800
1000
Temperature (K)